METHODS FOR DOSE CALCULATION AND BEAM CHARACTERIZATION IN EXTERNAL PHOTON BEAM RADIOTHERAPY

Doctoral Dissertation

Laura Korhonen

Helsinki University of Technology
Faculty of Information and Natural Sciences
Department of Biomedical Engineering and Computational Science

METHODS FOR DOSE CALCULATION AND BEAM CHARACTERIZATION IN EXTERNAL PHOTON BEAM RADIOTHERAPY

Doctoral Dissertation

Laura Korhonen

Dissertation for the degree of Doctor of Science in Technology to be presented with due permission of the Faculty of Information and Natural Sciences for public examination and debate in Auditorium of Engineering Physics at Helsinki University of Technology (Espoo, Finland) on the 27th of November, 2009, at 12 noon.

Helsinki University of Technology
Faculty of Information and Natural Sciences
Department of Biomedical Engineering and Computational Science

Teknillinen korkeakoulu
Informaatio- ja luonnontieteiden tiedekunta
Lääketieteellisen tekniikan ja laskennallisen tieteen laitos

Author   Laura Korhonen

Name of the dissertation

Methods for dose calculation and beam characterization in external photon beam radiotherapy

Abstract

Treatment planning in external photon beam radiotherapy requires fast and accurate methods for the calculation of an absorbed dose distribution in a patient. Modern dose calculation algorithms also require characterization of the radiation beam produced by a medical linear accelerator.

In this thesis, a dose calculation method based on the superposition of Monte Carlo simulated pencil-beam kernels was developed. The pencil-beam is divided into a depth-directed and a lateral component, which are separately scaled according to the radiological path-length information to account for tissue heterogeneities. The scatter along the plane is computed efficiently using incremental methods. In addition, a physics-based multiple-source model was developed in order to model the radiation beam. The free parameters of the model are derived using an automatic process, which minimizes deviations between the dose computations and the water-phantom measurements. The beam model was also incorporated with a Monte Carlo (MC) based dose calculation method.

The accuracy of developed kernel-based dose calculation method and beam model were verified by performing comparisons to measurements in a wide range of conditions including irregular, asymmetric, wedged and IMRT fields. In heterogeneous phantoms containing lung and bone inserts, the accuracy was also investigated using MC simulations. The deviations between the dose calculations and measurements or MC simulations were within the clinical acceptability criteria in most of the studied cases with the exception of a high-energy beam with small dimensions in a low-density material. However, the obtained accuracy in the problematic cases was still significantly better than that of a currently widely used semi-empirical method. The dose calculations with the developed MC based system also agreed with water-phantom measurements within 2%/2 mm for open fields and within 3%/3 mm for wedged fields.

Thus, the dose calculation algorithm and beam model developed in this thesis were found to be applicable for clinical treatment planning of megavoltage photon beams. In addition, it was demonstrated that the beam model can be successfully used as an input for other modern dose calculation methods, such as the Monte Carlo method.

VÄITÖSKIRJAN TIIVISTELMÄ	TEKNILLINEN KORKEAKOULU PL 1000, 02015 TKK http://www.tkk.fi

Tekijä	Laura Korhonen

Väitöskirjan nimi

Menetelmiä annoslaskentaan ja säteilykeilan mallinnukseen ulkoisessa fotonisädehoidossa

Käsikirjoituksen päivämäärä	25.8.2009	Korjatun käsikirjoituksen päivämäärä	25.10.2009

Väitöstilaisuuden ajankohta	27.11.2009

☐ Monografia   ☒ Yhdistelmäväitöskirja (yhteenveto + erillisartikkelit)

Tiedekunta	Informaatio- ja luonnontieteiden tiedekunta
Laitos	Lääketieteellisen tekniikan ja laskennallisen tieteen laitos
Tutkimusala	Lääketieteellinen tekniikka
Vastaväittäjä(t)	Adjunct Professor Anders Ahnesjö, Uppsala University
Työn valvoja	Professori Pekka Meriläinen
Työn ohjaaja	TkT Sami Siljamäki

Tiivistelmä

Ulkoisen sädehoidon suunnittelemiseksi fotonisäteilyä käyttäen tarvitaan nopeita ja tarkkoja menetelmiä, joilla lasketaan (ennustetaan) potilaaseen absorboituva annosjakauma. Nykyaikaiset annoslaskentamenetelmät edellyttävät myös lineaarikiihdyttimen tuottaman säteilykeilan mallintamista.

Tässä väitöskirjassa esitetään annoslaskentamenetelmä, joka perustuu Monte Carlo (MC)-menetelmällä simuloitujen kapeiden säteilykeilojen superpositioon. Menetelmässä kapea keila jaetaan syvyys- ja sivusuuntaisiin komponentteihin, mikä mahdollistaa kudoksen epätasaisen elektronitiheysjakauman huomioimisen, sillä kumpaakin komponenttia voidaan erikseen muuttaa radiologisen polunpituusinformaation perusteella. Tasossa tapahtuva sironta lasketaan tehokkaasti inkrementaalisilla menetelmillä. Lisäksi väitöskirjassa esitetään fysikaalinen monilähdemalli kiihdyttimen tuottaman säteilykeilan kuvaamiseksi. Mallin vapaat parametrit saadaan määrättyä automaattisella menetelmällä, jossa minimoidaan lasketun annoksen ja vesifantomissa mitatun annoksen eroja. Kehitetty säteilykeilan malli yhdistettiin myös MC-pohjaiseen annoslaskentamenetelmään.

Kehitetyn annoslaskentamenetelmän ja säteilykeilan mallin tarkkuus varmennettiin tekemällä mittavertailuja laajalla testijoukolla, johon kuului epäsäännöllisiä, epäsymmetrisiä, kiila- ja intensiteettimuokattuja kenttiä. Laskennan tarkkuutta heterogeenisissä fantomeissa, joissa oli keuhkoa ja luuta simuloivaa materiaalia, tutkittiin myös MC-menetelmiä käyttäen. Havaitut poikkeamat laskennan ja mittausten tai MC-simulaatioiden välillä täyttivät useimmissa tapauksissa kliiniset hyväksymiskriteerit, poikkeuksena pieni kenttä suurienergisessä säteilykeilassa keuhkossa. Tästä huolimatta saatu tarkkuus oli parempi kuin nykyään laajasti käytössä olevalla puoli-empiirisellä menetelmällä. Kehitetyllä MC-pohjaisella laskentajärjestelmällä saadut tulokset täsmäsivät vesifantomimittausten kanssa 2%/2 mm tarkkuudella avokentille ja 3%/3 mm tarkkuudella kiilakentille.

Esitetty annoslaskentamenetelmä ja säteilykeilan malli soveltuvat kliiniseen fotonikeilojen annossuunnitteluun. Väitöskirjassa osoitettiin myös, että kehitetty säteilykeilan malli on mahdollista yhdistää muihin nykyaikaisiin potilasannoslaskentamenetelmiin (esim. Monte Carlo).

Asiasanat	annoslaskenta, optimointi, superpositio, sädehoito, säteilykeilan mallinnus

ISBN (painettu)	978-952-248-173-3	ISSN (painettu)	1795-2239
ISBN (pdf)	978-952-248-174-0	ISSN (pdf)	1795-4584
Kieli	englanti	Sivumäärä	88 + 88 (liitteet)

Julkaisija	Lääketieteellisen tekniikan ja laskennallisen tieteen laitos, Teknillinen korkeakoulu

Painetun väitöskirjan jakelu	Lääketieteellisen tekniikan ja laskennallisen tieteen laitos

☒ Luettavissa verkossa osoitteessa http://lib.tkk.fi/Diss/2009/isbn9789522481740/

Preface

The author of the thesis was known as Laura Tillikainen until August 8th, 2009 when her name changed to Laura Korhonen in marriage.

The work for this thesis has been carried out at Varian Medical Systems Finland during the years 2004-2008. I am grateful for Varian for having the possibility to perform this interesting research, to write scientific publications about the theory and results. The research at Varian has largely been performed in a group. Therefore, I want to thank my ex-coworkers Hannu Helminen and Jyrki Alakuijala and current co-workers Sami Siljamäki and Tuomas Torsti for their contributions to the methods presented in this thesis. I want to express my gratitude to Katja Pesola and Joakim Pyyry for the continuous support given to me for the PhD studies. I also want to acknowledge Ann Van Esch and Dominique Huyskens for providing excellent quality measurements that were used in the development and verification of the methods, and also for their help in preparing the journal manuscripts.

I want to thank my supervisor, professor Pekka Meriläinen, for his support during the years and for the useful comments about the thesis. I express my gratitude to my instructor, Dr. Sami Siljamäki, for the well-thought and thorough remarks. I am most grateful to the official pre-examiners of the thesis, Docent Simo Hyödynmaa and Docent Jani Keyriläinen, for their valuable comments during the preparation of the final manuscript. I also appreciate my husband Teemu Korhonen for his continuous support and useful practical advices for typesetting of the text and presentation of the figures in LaTeX.

Finally, I acknowledge Finnish Cultural Foundation (Suomen Kulttuurirahasto) and the Education Fund (Koulutusrahasto) for the financial support during my study leave.

Espoo, October 2009

Laura Korhonen (née Tillikainen)

Contents

List of Publications

This thesis consists of an overview and of the following publications, which are referred in the text by their Roman numerals:

I L. Tillikainen, H. Helminen, T. Torsti, S. Siljamäki, J. Alakuijala, J. Pyyry and W. Ulmer. A 3D pencil-beam-based superposition algorithm for photon dose calculation in heterogeneous media. *Physics in Medicine and Biology*, 53:3821-3839, 2008.

II L. Tillikainen, S. Siljamäki, H. Helminen, J. Alakuijala and J. Pyyry. Determination of parameters for a multiple-source model of megavoltage photon beams using optimization methods. *Physics in Medicine and Biology*, 52:1441-1467, 2007.

III A. Van Esch, L. Tillikainen, J. Pyykkönen, M. Tenhunen, H. Helminen, S. Siljamäki, J. Alakuijala, M. Paiusco, M. Iori and D. P. Huyskens. Testing of the analytical anisotropic algorithm for photon dose calculation. *Medical Physics*, 33:4130-4148, 2006.

IV L. Tillikainen and S. Siljamäki. A multiple-source photon beam model and its commissioning process for VMC++ Monte Carlo code. *Journal of Physics: Conference Series*, 102:012024, 2008.

V L. Tillikainen. Multi-source modeling of flattening filter free photon beams. *Conference Proceedings for the XVth International Conference on the Use of Computers in Radiation Therapy*, pp. 408-412, 2007.

Author's Contribution

In **I**, the author presents a method to calculate the 3D dose distribution in the patient for megavoltage photon beam radiotherapy. The author contributed substantially to the development of the calculation method, prepared the data for the results section, and had the primary responsibility for the production of the manuscript.

In **II**, the author describes a multiple-source model to characterize the radiation output of a medical linear accelerator. In addition, a method to derive the free parameters of the model from simple radiation measurements using optimization methods is described. The model is designed to be used together with the dose calculation method of **I**. The author had a major contribution to the development of the described methods, and also had the primary responsibility for the production of the manuscript.

In **III**, an overview of the dose calculation method developed in **I** and of the beam characterization techniques developed in **II** is given. Then, clinical acceptance tests for the methods integrated into the Eclipse$^{\mathrm{TM}}$ Integrated Treatment Planning System are presented. In these tests, the calculation results of a new method (Anisotropic Analytical Algorithm), are compared against dosimetric measurements and calculations with a currently used method (Pencil Beam Convolution) in a wide range of conditions. The author was responsible for the algorithm description in the manuscript, and contributed to the analysis of the results.

In **IV**, the author describes how the methods developed in **II** can be applied for the beam modeling for a Monte Carlo based dose calculation algorithm. The techniques to convert the model to a form, which is suitable for Monte Carlo based algorithm, are described. The calculation results in several conditions are benchmarked against dosimetric measurements. The author contributed significantly to the development of the described methods, and also had the primary responsibility for the production of the manuscript.

In **V**, the author applies the methods developed in **I** and **II** to the beams not having the flattening filter component in the beamline (unflattened beams). The author was solely responsible for the production of the manuscript.

List of Abbreviations

2D	Two-dimensional
3D	Three-dimensional
AAA	Anisotropic Analytical Algorithm
CAX	Central axis
CPE	Charged particle equilibrium
CT	Computerized tomography
DNA	Deoxyribonucleic acid
DTA	Distance-to-agreement
EDW	Enhanced dynamic wedge
FFF	Flattening filter free
IMRT	Intensity modulated radiotherapy
Kerma	Kinetic energy transferred per unit mass
Linac	Linear accelerator
MC	Monte Carlo
MLC	Multi-leaf collimator
MSM	Multiple-source model
MU	Monitor unit
PDD	Percentage depth dose
PBC	Pencil beam convolution
RT	Radiotherapy
SAR	Scatter-air ratio
SDD	Source-to-detector distance
SSD	Source-to-surface distance
TAR	Tissue-air ratio
TG	Tongue-and-groove
TCPE	Transient charged particle equilibrium
TMR	Tissue-maximum ratio
TPS	Treatment planning system
VMC	Voxel Monte Carlo

List of Symbols

c	Speed of light in vacuum
m	Mass
h	Planck's constant
ν	Frequency of electromagnetic radiation
Z	Atomic number
ρ	Density
μ	Linear attenuation coefficient
μ_{tr}	Energy transfer coefficient
μ_{en}	Energy absorption coefficient
Φ	Particle fluence
Φ_E	Particle fluence spectrum
Ψ	Energy fluence
Ψ_E	Energy fluence spectrum
E_{tr}	Energy transferred to charged particles in photon interactions
E_{en}	Energy deposited by charged particles released in photon interactions
g	Radiative fraction
R	Maximum range of secondary electrons
K	Kerma
K_c	Collision kerma
K_r	Radiative kerma
D	Absorbed dose
Q	Charge
W_{air}	Mean energy required to produce an ion pair in air
e	Electron charge
S	Stopping power
S_{col}	Collision stopping power
ϵ	Energy imparted by ionizing radiation
λ	Photon mean free path
d_{eff}	Effective (radiological) distance
d_{max}	The depth of maximum dose in depth dose curves
$h_\beta(r, z)$	Polyenergetic pencil-beam kernel
$I_\beta(z)$	Depth-directed component of the pencil-beam
$k_\beta(r, \theta, z)$	Lateral component of the pencil-beam
ρ_{w}	Electron density relative to water
$I(r)$	Intensity profile
$\bar{E}(r)$	Mean radial energy
σ	Standard deviation of a Gaussian distribution

17

1 Introduction

Radiation therapy (radiotherapy, RT) is a commonly used and efficient method for cancer treatment, where ionizing radiation is used in an attempt to kill the malignant tumor cells or to slow down their growth. It is often combined with surgery, chemotherapy, or hormone therapy, but may also be used as a primary therapy mode. RT is not limited to the treatment of malignant diseases, but can be used to treat benign neoplasms, such as trigeminal neuralgia. Internal RT or brachytherapy uses sealed or unsealed radioactive sources, which are placed near the treatment area either temporarily or permanently. In the latter form of therapy, medication containing radioactive materials is injected into a vein or a body cavity. External beam RT, on the other hand, uses radiation beams produced by sources located outside the patient. The beam can consist of photons, electrons, protons or other heavy ions; photons being the most commonly used particle type at present. In this thesis, methods for modeling the megavoltage photon beams used in external beam RT are described, whereas the electron, proton and heavy ion beams are not in the scope of this thesis.

The genomic deoxyribonucleic acid (DNA) of malignant cells is damaged by the ionizing radiation used in RT. There are various types of DNA lesions that are inflicted either by direct ionization or via free radicals generated in the cells as a result of the irradiation. Double strand break of the DNA correlates best with cell death. Usually, most of the lesions in the DNA are rapidly repaired by enzymatic pathways in the cell. However, sometimes the cells are unable to completely or accurately repair the DNA damage leading to a mutation or a cell death after a variable number of cell cycles. This mode of the cell death is called mitotic or clonogenic cell death, and it is the major mechanism of tumor response in RT. An alternative mode of cell death is apoptosis, which has significantly lower occurrence in most of the cancer types. The DNA damage caused by radiation naturally occurs also in healthy cells, but due to faster reproduction and poorer DNA repair capabilities, cancer cells are more sensitive to ionizing radiation. [1]

1.1 A short history of external photon beam radiotherapy

The history of external photon beam RT starts from the discovery of x-rays by Wilhelm C. Röntgen in 1895. The first empirical cancer therapy with x-rays was performed only a few months after the first report of the finding [2]. Radioactivity was discovered by Henri Becquerel in 1896, which was followed by the discovery of radium by Marie and Pierre Curie in 1898. Since these discoveries, the field of RT began to grow as radium based treatment techniques became available. In principle, during the first three decades, the RT was practised by only a few specialists who

varied different treatment parameters (e.g. dose, field size, position) according to their experience and patients' daily condition [3]. It was not until the beginning of 1940s, when the basic principles of modern RT were established, and the treatments became more quantitative and more easily specified. These principles stated that it is necessary to determine the size, shape and position of the volume to be treated, and that this volume should receive as uniform (pre-determined) dose distribution as possible [3]. It was also understood that the dose to healthy tissues outside the treatment volume should be minimized, and that it is important to give consistent treatments for patients with similar disease type in order to gather information about proper dose levels. Current RT is largely based on the above mentioned principles [3].

External beam RT treatment units developed from the early radium-226 teletherapy units in 1920s, through 700–800 kV orthovoltage units in 1930s, eventually to 1.25 MeV (average energy) cobalt-60 units in 1950s [2]. Since the introduction of a 6 MV medical linear accelerator (linac) in 1953 [4], the practicality and efficiency of multi-field RT treatments were dramatically increased. The improvements were due to the significant increase in the percentage depth dose (PDD) curves and reduced scattering compared to the kilovoltage x-ray radiation, which enabled the utilization of fewer and better defined treatment fields [3]. This in turn lead to a reduced dose to normal tissues and better cure rates. The linac has the distinct advantage of being free of periodically replaceable radioactive radiation source. Instead, the x-rays are produced by accelerating electrons in a waveguide, and letting them collide with a thin metallic plate, the so-called x-ray target. The bremsstrahlung radiation produced by the impinging electron beam is then used for the treatment. Today, medical linacs may have several energy modes (accelerating voltages) ranging from 4 MV to 25 MV. Linac has largely replaced earlier devices in external beam RT, although cobalt-60 units are still used especially in the developing countries mainly due to their easy maintenance. X-ray beams of cobalt-60 radiation are still used for special radiosurgery purposes, such as in the Gamma Knife device. It has a set of cobalt-60 sources placed in a spherical array in a shielded assembly, and is capable of focusing the radiation precisely to the tumor [5]. A modern medical linac is shown in Fig. 1(a) and a diagram of its major components in Fig. 1(b).

After the invention of medical linac, major advancements in RT have been made in the area of treatment planning, and in the related field of computer controlled hardware. The multi-leaf collimator (MLC) which appeared in the market in 1980s, made it easier to deliver fields conforming to the projection of the target [7]. In more advanced applications, the individual leaves of the MLC are moved separately in a computer control at desired speeds during beam-on. This enables the generation of spatially modulated radiation fields, since each leaf attenuates the beam for a different time period. The resulting intensity modulated radiotherapy (IMRT) has
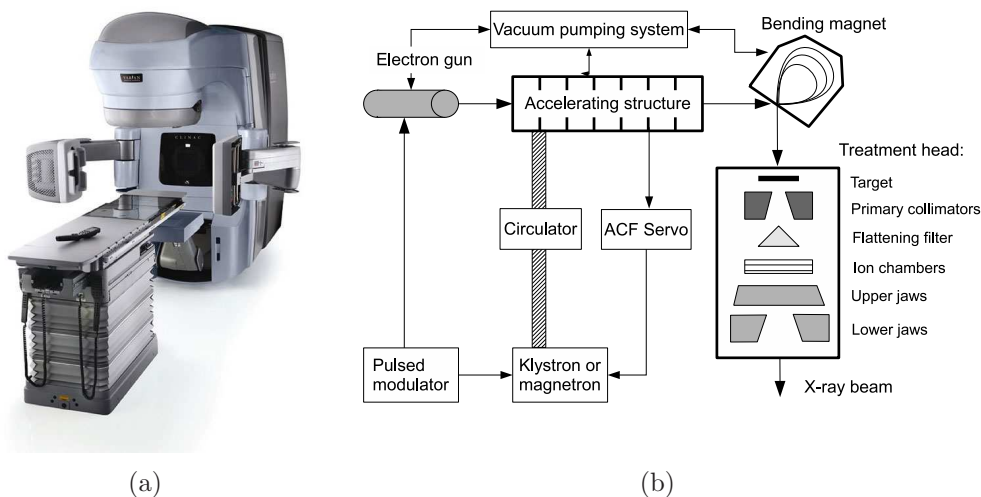
<div align="center">(a)   (b)</div>

Fig. 1: (a) Varian Clinac® iX linac (image used with permission, © Varian Medical Systems Inc., all rights reserved). (b) The main components of the linac (modified from [6]).

enabled the creation of high dose volumes that conform more closely to the shape of complicated targets. The integration of x-ray image receptors to the linac has enabled the imaging of the patient before each treatment session and the tracking of tumor motion during treatment delivery. These so-called image-guided RT methods have improved patient positioning accuracy, and have lead to techniques for restricting tumor motion during treatment.

1.2   Treatment planning for radiotherapy

In RT treatment planning, the purpose is to devise a treatment, which produces as uniform dose distribution as possible to the target volume and minimizes the dose outside this volume. In RT planning, the beam qualities, field sizes, positions, orientations and relative weights between the fields are typically modified. It is also possible to add certain accessories (e.g. wedge filters or blocks) to the fields to account for inclined patient surface or to shield critical structures from radiation exposure.

Practising of treatment planning started in 1940s, when the developments in radiation dosimetry enabled each clinic to measure the isodose charts for any type of treatment field, thus enabling manual 2D planning [3]. To avoid laborious isodose measurements, empirical methods for the calculation of dose distribution were developed later [8, 9]. Computer-based treatment planning systems (TPSs) first conceptualized in 1955, allowed the planner to see the effect of the beam modifications immediately on the predicted dose distribution. This resulted in better quality plans, since it became easier to experiment with a larger set of treatment parameters. A real breakthrough for RT was the introduction of the computerized tomography (CT) scanner in 1970s, which enabled acquiring detailed 3D anatomical information
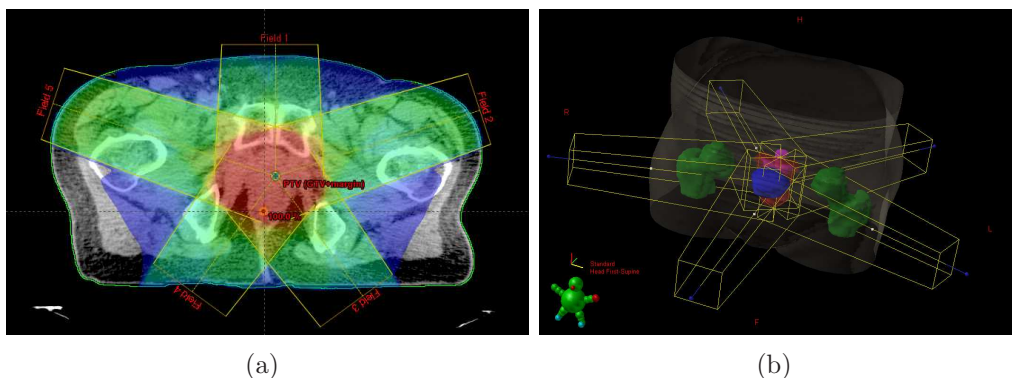
<div align="center">21</div>

Fig. 2: (a) A transversal plane of a five-field coplanar prostate plan generated in Eclipse^{TM} TPS. The calculated dose distribution is shown as a colormap superimposed on the CT image. The radiation beams intersect in the region of the tumor in order to spare the healthy tissue in the regions where the beam enters or exits patient. (b) A 3D view of the contoured organs and a field geometry in Eclipse^{TM}, (images used with permission, ©Varian Medical Systems Inc., all rights reserved).

of the patient. Within a few years, CT scans were routinely used as an input for the treatment planning process [2], resulting in a 3D view of the dose distribution (see Fig. 2). Other new imaging modalities, such as the magnetic resonance imaging and positron emission tomography, provided help in more accurate determination of anatomical details and extent of a lesion. The latter modalities can be used in treatment planning by registering them to the CT coordinate system with the aid of specially designed image registration algorithms. Inverse-planning methods that have become available in 1990s, aim at generating an optimal beam arrangement based on certain objectives set for target and normal tissue doses. For example in IMRT, the inverse-planning system optimizes the leaf motion patterns to meet the desired dose-volume or radiobiological objectives.

1.3 Dose calculation methods

Currently, it is practically not possible to obtain a direct measurement of the 3D dose distribution delivered to a patient. Therefore, the treatment planning has to be based on calculation models. Even if direct measurements were possible, it would still be much more practical and convenient to perform planning based on calculation models. The dose predicted by a calculation method should correspond to the real absorbed dose in the patient as accurately as possible. The dose received by the tumor volume should be close to the prescribed dose level, which by experience has been shown to yield the best outcome for the particular cancer type. Certain organs have critical dose levels that should not be exceeded, or otherwise serious side-effects could occur. Accurate dose calculation is also necessary in order to further improve our understanding of the biological response mechanisms in RT, since the calculated dose must be used in reporting and further correlating the tumor responses to certain

dose levels. In addition, the biological response of cells to radiation is highly non-linear, and therefore small errors in the predicted dose may lead to large errors in prediction of the biological response [10]. Nevertheless, it should be noted that the dose calculation methods are not the only source of error between the predicted and the delivered dose distributions: beam and patient positioning, patient movement and deformation, as well as the stability of the treatment unit contribute significantly to the overall error.

Methods based on empirical formulae, such as [9], were the first techniques developed for dose calculation. In these methods, the primary and scattered radiation components are treated separately, since they have different physical behaviour in a material. The primary component describes the distribution of the energy deposited by the first photon interaction in the material, and the scatter component describes the result of the subsequent interactions, which distribute the energy away from the first interaction site. In the method presented by J. R. Cunningham [11], the scatter is computed with the help of a scatter-air ratio (SAR), which is derived from a measured tissue-air ratio (TAR) and its extrapolation to a zero-area beam. Handling of irregular field shapes is typically based on the integration method developed by J. R. Clarkson [8], where the field around the calculation point is divided into a number of angular segments. The dose contribution of each segment is estimated from the scatter function (e.g. SAR), and the contributions are summed up. Later more elaborate semi-empirical methods were developed, which derive scatter kernels from measured beam data [12, 13]. However, all the empirical and semi-empirical methods have difficulties to model generalized beam setups.

Various methods have been developed to account for the fact that the tissue density differs from the water density. Commonly, the dose distribution calculated for the homogeneous water-equivalent situation is converted into the heterogeneous situation in the same geometry by applying a point-by-point correction factor. Most methods, such as the equivalent path-length method(s) [10] or the Batho power-law method [14], determine the correction factor by a direct ray-tracing from the primary radiation source to the point of interest. More sophisticated techniques, such as the equivalent TAR method [15,16], use the electron density data from the CT image to determine the correction factors. The use of these correction factors may still lead to deviations up to 10% from the measured dose for certain type of geometries.

Kernel-based or convolution/superposition dose calculation methods are based on physical principles of the radiation behaviour rather than on direct beam data measurements. Energy deposition kernels can be used to model the photon transport, since the energy deposition around the primary interaction site is independent of the position of the site in homogeneous media. Kernel-based methods are able to compute the dose directly for irregular photon beams in heterogeneous phantoms. Non-water equivalent tissues are typically taken into account by scaling the kernels

23

with the mean electron density between the interaction point and the dose calculation point [10]. In the 3D point-spread kernel methods [17–20], the dose deposition can be viewed as a superposition of appropriately weighted responses to point irradiations. If the kernels are spatially invariant, these superpositions can be computed by means of convolution to achieve high computational efficiency [10]. However, the point-spread kernel methods are typically still computationally expensive. In order to overcome this problem, other methods based on the superposition of 2D pencil-beam kernels have been developed [21–24]. When using the 2D pencil-beam kernels, the heterogeneities cannot be fully corrected, but the calculation times can be significantly smaller than in the 3D point-spread kernel based methods. Both the point-spread and pencil-beam kernels are usually derived from Monte Carlo (MC) simulations, although some authors have used analytical expressions to compute the first and multiple scatter kernels [18, 25]. The kernel-based methods have been proven to be more accurate than the empirical methods, but still have limitations in modeling the situations of severe lateral electronic disequilibrium, such as a small sized field of a high energy beam inside lung tissue [26].

The MC methods, such as those presented in [27, 28], are generally regarded as the most accurate methods currently available for dose calculation. These methods explicitly model each photon interaction in the patient. Usually, however, a number of electron (Coulomb) interactions are grouped together and modeled using the so-called condensed history technique [29, 30]. The interactions are modeled via random sampling from the cross-section distributions for each type of interaction. MC methods are widely used to study radiation beam properties and to benchmark other dose calculation methods, but until recently they have been too slow to be used in routine treatment planning. Recent advancements in computer technology and variance reduction techniques may change the situation in the near future. Another way to generate accurate dose distribution is the to solve directly the coupled photon and electron transport equations (Boltzmann equations) by using sophisticated discretization methods [31, 32]. Even in the presence of very accurate dose calculation methods, faster methods are still needed e.g. for inverse-planning and for interactive manual planning.

All the modern dose calculation algorithms, including the kernel-based and MC methods, require a characterization of the radiation produced by the linac. Kernel-based methods require information about the energy spectrum and energy fluence of the primary beam, and radiation scattered from the linac head components. Also the presence of electron contamination in a photon beam must be modeled. These techniques developed for modeling the radiation beam are often called beam characterization or source modeling techniques. An accurate method to characterize the treatment beam is to perform a full MC simulation through the treatment head components, and score the particles on a plane below the last collimating device to

a so-called phase-space file [33, 34]. However, this approach requires detailed information about the geometry and composition of the various linac head components, which may not be easily achievable from the manufacturers. In addition, the properties of the initial electron beam, which is hitting to target, are not known with sufficient accuracy. Thus, the modification of e.g. the electron beam energy and spot size to match an individual treatment unit is a non-trivial and time-consuming process [35].

Other methods create histograms from the MC simulated phase-space for energy fluences and spectra [36–38]. The benefit of these methods compared to the full simulation approach is the significantly smaller storage space requirement. Analytical or virtual source model approaches — on the other hand — construct parameterized models of the photon and electron energy fluences and spectra for two or more subsources in the beam [39–43]. These multiple-source models (MSMs) usually require only limited technical information about the linac construction. Free parameters for the functions describing e.g. the energy fluence can be obtained by fitting to the MC simulated phase-space data or can be derived from measurements using optimization techniques. The latter approach allows easy adaptation of the model to different treatment units. The analytical models may not be as accurate as the full MC approach, if all the relevant physical phenomena are not taken into account in the model design. If the model parameters are derived from the measurements, particular care should be taken in order to avoid the characterization of noise or measurement artifacts. These problems can be alleviated by designing a physics-based model and using certain restrictions when optimizing the parameter values.

A modern dose calculation system intended for routine treatment planning should address the following challenges:

1. The calculation model should be applicable to generalized beam setups, including irregularly shaped beams and varying source-to-surface distances (SSDs).
2. The effects of oblique patient skin and heterogeneous tissue on primary and scattered radiation components should be accurately modeled.
3. The radiation beam produced by the medical linac should be characterized using only a limited set of technical information.
4. The beam model should be adaptable to an individual treatment machine.
5. The computation time should be short enough to facilitate interactive planning.

1.4 Aims of the thesis

The aims of this thesis are summarized in the table below. The methods developed in this thesis attempt to solve the dose calculation related problems presented in Sec. 1.3.

	Aim	Publication
1.	To develop a dose calculation method based on MC simulated pencil-beam kernels and integrate it as a part of a commercial TPS.	**I**
2.	To create a model to characterize the radiation beam produced by a linac. The model shall be easily adaptable to an individual treatment machine, and shall provide suitable input for the kernel-based dose calculation method.	**II**, **V**
3.	To verify the accuracy of the developed dose calculation method and beam model using a comprehensive set of measurements and MC simulations in clinically relevant beam geometries and phantoms.	**I**, **III**
4.	To incorporate the developed beam model with a MC based patient dose calculation method, and verify the accuracy of the model in this context.	**IV**

The main goal of the thesis was to develop a kernel-based algorithm, which would have similar computation time as the existing Pencil Beam Convolution (PBC) algorithm has [13], but would have better accuracy in generalized beam setups and in heterogeneous media. The improvements in the accuracy are possible due to the more physics-based approach on both the dose calculation and the beam modeling, as was shown in **III**. The methods described in **I** and **II** have been implemented as the AAA algorithm in the Eclipse™ Integrated TPS. Another goal for developing the beam model presented in **II** was the possibility to utilize the same model as an input for a MC based dose calculation method as was done in **IV**. This makes the potential future implementation of a MC algorithm in a commercial planning system easier. Since the developed beam model is quite flexible for adapting to different beams, it was also applied for the modeling of unflattened or flattening filter free (FFF) beams in **V**. These beams are expected to be used more frequently in the future, since the beam-on time and scatter contribution to normal tissues can be potentially reduced compared to the use of conventional beams.

2 Background

In this chapter, some background information about the transport mechanisms of photons in matter is given, and basic quantities used in characterizing radiation are defined. Finally, basics of ion chamber dosimetry and most common experimental quantities are presented.

2.1 Radiation transport in material

Photons ionize matter indirectly; photon interactions in a medium release charged particles (electrons or positrons), which in turn deposit energy through direct Coulomb interactions with the orbital electrons of the atoms. The intensity of a monoenergetic photon beam incident on a layer of material attenuates according to the exponential attenuation law [44]:

$$I(x) = I_0 e^{-\mu(E)\,x}, \tag{2.1}$$

where I_0 is the initial photon intensity before entering the material, E the energy of the photons, μ the linear attenuation coefficient for the material in question, and x the material thickness. Eq. (2.1) is valid for a narrow beam geometry where the scattered particles do not reach the detector, or alternatively for the primary component of a broad photon beam where the scattered particles are not counted for in $I(x)$. Mass-attenuation coefficient μ/ρ is also a commonly used quantity in the literature, and is formed by dividing the linear attenuation coefficient with the mass density of the medium. The linear attenuation coefficient μ is the sum of the attenuation coefficients of the various interactions, i.e. [44]:

$$\mu = \tau + \sigma_R + \sigma_C + \kappa, \tag{2.2}$$

where τ denotes the coefficient for photo-electric effect, σ_R for Rayleigh scattering, σ_C for Compton scattering, and κ for pair production. These are the most important photon interactions in the therapeutic energy range, although nuclear interactions also contribute to a small extent to μ for large photon energies (> 10 MeV).

2.1.1 Photon and electron interactions

In the photo-electric interaction, a photon interacts with a tightly bound orbital electron of an atom in the attenuating material. As a result of the interaction, the photon is absorbed and the orbital electron is ejected with kinetic energy equalling the incident photon energy subtracted by the electron binding energy (E_B). The linear attenuation coefficient of the photo-electric effect τ is proportional to $(Z/E)^3$, and is hence most common in low-energy photon interactions. [45]

In the Rayleigh (coherent) scattering process, the photon interacts with a bound orbital electron such that it loses essentially none of its energy, but is deflected to a small angle with respect to the incident direction. In tissue equivalent materials, the importance of Rayleigh scattering with respect to the other interaction types is small, contributing a maximum of a few percent to the total linear attenuation coefficient. [45]

In the Compton (incoherent) scattering, the photon interacts with an effectively free and stationary orbital electron ($E \gg E_B$). The photon loses part of its energy to the Compton (recoil) electron that is ejected from the atom. A photon with a smaller energy is then scattered through an angle, which is dependent on the amount of energy lost in the interaction. The Compton mass attenuation coefficient σ_C/ρ is independent of Z, and decreases slowly as a function of the photon energy. [45]

If a high-energy photon is located in the Coulomb field of a nucleus, a pair-production event may occur. In this interaction, the photon disappears and an electron-positron pair, both particles having a kinetic energy of $E - 2m_e c^2$, is produced (m_e is the rest mass of the electron). Hence, the energy threshold for pair-production is $2m_e c^2 = 1.02$ MeV. The mass attenuation coefficient for pair production κ/ρ is proportional to Z, and increases rapidly with photon energy above the threshold. Pair-production is followed by the annihilation of the positron with a free electron, producing two annihilation photons. The energy of these photons is typically 511 keV, but it can be somewhat larger if the annihilation occurs before the positron has lost all of its kinetic energy [45].

In tissue-equivalent materials, the photo-electric effect dominates for energies up to about 20 keV, the Compton scattering dominates in energy interval $0.02, \ldots, 10$ MeV, whereas the pair-production dominates for energies larger than about 10 MeV. The mass-attenuation coefficients in water for the above-mentioned three interactions types are shown in Fig. 3 for therapeutic energy range. [44, 45]

High-energy electrons interact with matter via Coulomb interactions with atomic orbital electrons and atomic nuclei. In these interactions, electrons may lose their kinetic energy (inelastic collision), or merely change their direction of movement (elastic collision). Typically, a high-energy electron undergoes thousands of interactions before coming to rest. This process is typically modeled using the statistical theory of multiple scattering. The type of the interaction an electron undergoes with an atom is dependent on the impact parameter b, which is the perpendicular distance from the direction of the electron movement before the interaction to the center of the atom. The radius of the atom is denoted with parameter a. If $b \gg a$, electron experiences a soft collision with the atom, where a small amount of energy is transferred to the orbital electrons and the electron movement direction changes slightly. If $b \approx a$, a hard collision between the electron and an orbital electron occurs, and large fraction of the initial electron energy is transferred to the orbital electron.
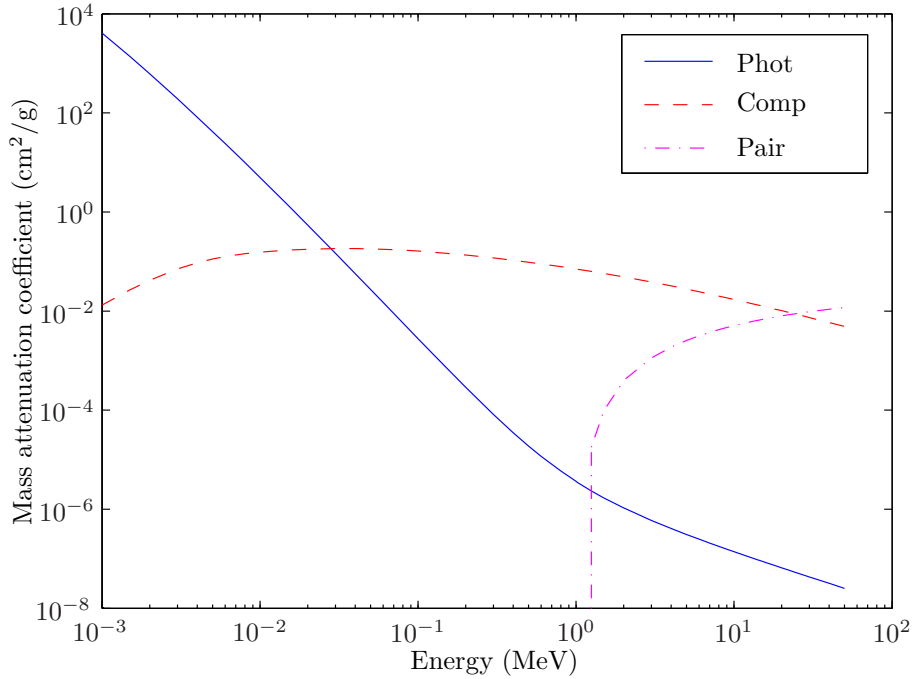
Fig. 3: Mass attenuation coefficients in water for the photo-electric effect (Phot), Compton scattering (Comp), and pair production (Pair). The data for this figure was obtained from [46].

If $b \ll a$, the electron undergoes a radiative interaction with the nucleus. In the latter case, the electron emits a bremsstrahlung photon having energy between zero and the kinetic energy of the incident electron; the smaller the impact parameter b, the larger the energy of the bremsstrahlung photon. [45]

2.1.2   Kerma, energy fluence and particle fluence

Two other attenuation coefficients are often defined in the literature: the energy transfer coefficient μ_{tr}, and the energy absorption coefficient μ_{en}. The energy transfer coefficient for a point P in the material is defined as [44]:

$$\mu_{\text{tr}}(E) = \mu \frac{\bar{E}_{\text{tr,p}}}{E}, \tag{2.3}$$

where $\bar{E}_{\text{tr,p}}$ is the average energy per photon transferred to charged particles at point P. Rayleigh scattering does not contribute to μ_{tr}, since the photon energy does not change during the interaction. The energy absorption coefficient at point P is analogously defined as [44]:

$$\mu_{\text{en}}(E) = \mu \frac{\bar{E}_{\text{en,p}}}{E}, \tag{2.4}$$

where $\bar{E}_{\text{en,p}}$ is the average energy per photon that is deposited by the charged particles created in P anywhere in the attenuating medium. These two quantities are related via [44]:

$$\mu_{\text{en}}(E) = (1-g)\mu_{\text{tr}}(E), \tag{2.5}$$

where g is the radiative fraction, which describes the average fraction of the transferred kinetic energy that is subsequently lost in photon-emitting energy-loss processes. Since g is dependent on the elements that are present within the maximum secondary electron range from P, μ_{en} is also dependent on the material composition surrounding P [47].

Kerma (acronym for kinetic energy transferred per unit mass) describes the transfer of energy from indirectly ionizing radiation to directly ionizing radiation at a specific location, but does not consider what happens to the particles afterwards. It is defined as [45]:

$$K = \frac{\mathrm{d}\bar{E}_{\text{tr}}}{\mathrm{d}m}, \tag{2.6}$$

where $\bar{E}_{\text{tr}}$ is the total kinetic energy transferred to ionizing particles within mass $\mathrm{d}m$. Kerma can be further divided into two components, the collision kerma K_c and radiative kerma K_r such that $K = K_c + K_r$. The division based on the type of the subsequent interactions the charged particles will undergo in the medium (collision interactions or radiative interactions). The collision kerma is defined as [44]:

$$K_c = (1-g)K = \frac{\mathrm{d}\bar{E}_{\text{en}}}{\mathrm{d}m}, \tag{2.7}$$

where g is the radiative fraction introduced in Eq. (2.5), and the radiative kerma is similarly defined as [44]:

$$K_r = gK. \tag{2.8}$$

For a monoenergetic photon beam, kerma is related to the mass energy transfer coefficient for the given energy as [44]:

$$K = \Psi \left[\frac{\mu_{\text{tr}}(E)}{\rho} \right], \tag{2.9}$$

where Ψ is the energy fluence of the monoenergetic photons. The energy fluence for a radiation beam having an arbitrary spectrum and composition of particles is defined as [44]:

$$\Psi = \frac{\mathrm{d}E}{\mathrm{d}A}, \tag{2.10}$$

where $\mathrm{d}E$ is radiant energy incident on a sphere with cross-sectional area $\mathrm{d}A$. In case of a monoenergetic photon beam, the energy fluence is related to the particle

fluence Φ via [44]:

$$\Psi = \frac{\mathrm{d}N}{\mathrm{d}A}E = \Phi E, \tag{2.11}$$

where $\mathrm{d}N$ is the number of particles incident on the area $\mathrm{d}A$, and $\Phi = \mathrm{d}N/\mathrm{d}A$ is the particle fluence. The definitions of particle and energy fluence consider an area $\mathrm{d}A$ perpendicular to the direction of each particle, so both are independent of the incident angle of the radiation. The photon beams in external beam RT are polyenergetic, and thus the concept of energy fluence spectrum Ψ_E is required [44]:

$$\Psi_E(E) = \frac{\mathrm{d}\Psi}{\mathrm{d}E}(E). \tag{2.12}$$

For the polyenergetic beams, the average mass energy transfer coefficient $\bar{\mu}_{\mathrm{tr}}/\rho$ is obtained as weighted sum from the monoenergetic coefficients μ_{tr}/ρ such that the spectrum $\Psi_E(E)$ determines the weight factor for each energy [44].

2.2 Basic theorems and principles

2.2.1 Inverse-square law

In external photon beam RT, the primary photon source located at the target is often assumed to be a point source. This source is irradiating to all directions downwards from the target, but with a forward-directed directional distribution. The collimating system of the treatment machine then shapes the radiation into a diverging beam with a well-defined, but possibly irregular, cross-sectional shape. A cross-section with area A at distance f_a from the point source is geometrically related to an area B at distance f_b as [45]:

$$\frac{A}{B} = \frac{f_a^2}{f_b^2}. \tag{2.13}$$

The number of photons emitted by the photon source that cross the area A, i.e. the photon fluence, is denoted by Φ_A. If no interactions occur in the air between between the planes at f_a and f_b, the same number of photons cross both areas. Hence, the following equality holds [45]:

$$\Phi_A A = \Phi_B B \Leftrightarrow \frac{\Phi_A}{\Phi_B} = \frac{B}{A} = \frac{f_b^2}{f_a^2}. \tag{2.14}$$

Eq. (2.14) implies that, in the absence of attenuation, the photon fluence is inversely proportional to the square of the distance from the source. The same relationship applies also for the energy fluence Ψ. This inverse-square law is utilized in dose calculations, when the distance of the calculation point from the source is changed.

2.2.2 Charged particle equilibrium

Dose calculation algorithms used in RT aim at predicting an absorbed dose distribution in a patient. The absorbed dose D to mass m in a finite volume V is defined as [48]:

$$D = \frac{\mathrm{d}\bar{\epsilon}}{\mathrm{d}m}, \tag{2.15}$$

where $\bar{\epsilon}$ is the expectation value of ϵ, the energy imparted by ionizing radiation to the mass m in the finite volume V. The unit of absorbed dose is gray (Gy), where 1 Gy = 1 J/kg. The energy imparted is given by [48]:

$$\epsilon = E_{\mathrm{in}} - E_{\mathrm{out}} + \Sigma Q, \tag{2.16}$$

where E_{in} is the radiant energy of all particles incident on the volume V, E_{out} is the radiant energy of all particles emerging from V, and ΣQ is the total energy gained or lost within V in mass-energy conversion processes. Radiant energy is the energy of particles that is emitted, transferred or received, excluding the rest-mass energy. For example, a pair production event taking place within V, where both the electron and the positron escape the volume, decreases the amount of emerging radiant energy by $2m_e c^2$. In this case, a negative term of the same magnitude needs to be included in ΣQ.

Charged particle equilibrium (CPE) exists with respect to volume V if for each charged particle of a given type, energy and direction leaving V, there is an identical particle entering V, in terms of expectation values [48]. This means that the net local physical effect G_l produced by the electron fluence in V is identical to the net effect G_d which is produced in the medium along the tracks of electrons arising from V [49]. The equality $G_d = G_l$ must be valid for all physical phenomena of the charged particles, although energy exchange is the most commonly studied phenomenon (see Fig. 4(a)). In energy exchange, G_l represents the absorbed dose D, and G_d represents the collision kerma K_c defined in Eq. (2.7), i.e. $D = K_c$ under CPE conditions [48]. Hence, if CPE holds, the average energy imparted ($\bar{\epsilon}$) equals the average energy deposited by the charged particles ($\bar{E}_{\mathrm{en}}$). Generally these two quantities differ, since transfer of energy to charged particles (kerma) does not lead to the absorption of the energy at the same location (dose). This is because secondary electrons released in the photon interactions have a finite range in the medium and deposit their energy along the entire track. The relationship between $\bar{\epsilon}$ and $\bar{E}_{\mathrm{en}}$ (or dose and kerma) in non-CPE conditions is illustrated in Fig. 4(b).

In a medium irradiated by photons, CPE is achieved in a point within a spherical volume of radius R, which equals the maximum range of secondary electrons, if the following two conditions are met: (1) the photon radiation must have spatially invariant intensity, energy spectrum, and angular distribution, and (2) the medium
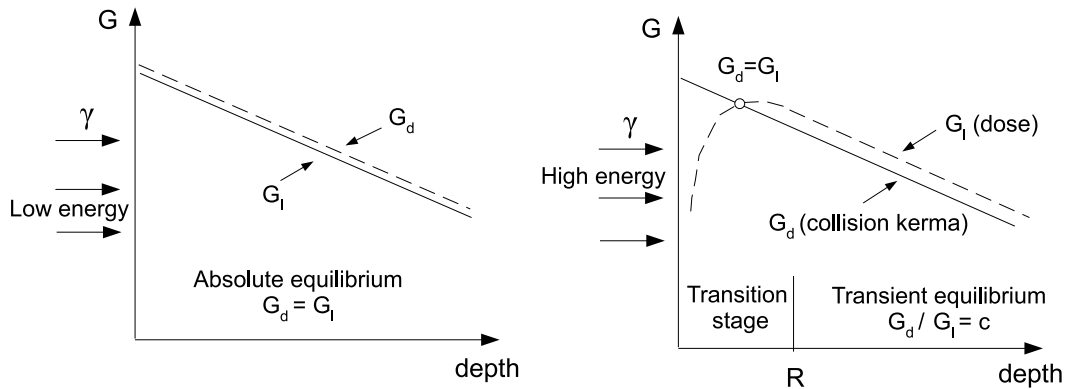
Fig. 4: (a) For a low-energy photon irradiation, an absolute charged particle equilibrium (CPE) practically exists throughout the irradiated volume. (b) In a high-energy photon beam, only a transient charged particle equilibrium (TCPE) is reached at depths larger than the maximum secondary electron range R, (modified from [49]).

must be homogeneous [49]. If the above conditions are met, $G_d = G_l$, and an *absolute equilibrium* exists. The first condition is practically fulfilled, if the beam divergence as well as the photon absorption and scattering are negligible over distances in the order of $2R$. It also follows that the point of interest must be further than distance R from the edge of the beam. The second condition requires that the point of interest to be further than distance R from any material interfaces and the edge of the irradiated body.

For low energy photons (e.g. $h\nu = 50$ keV), these conditions are practically fulfilled throughout the irradiated volume, since the mean free path of photons in water, denoted by $\lambda = 1/\mu$, is significantly larger than the maximum range of secondary electrons ($\lambda = 4.7$ cm, $R = 30$ μm, and $\lambda/R \approx 160$) [49]. In this case, as shown in Fig. 4(a), G_l and G_d are practically identical and decrease simultaneously as a function of depth. For photon energies higher than approximately 1 MeV, the above conditions are not fulfilled anywhere in medium, and the largest difference between G_l and G_d occurs near the surface (air-water transition stage) as shown in Fig. 4(b). In this region, the absorbed dose builds up in a few centimetre region close to the air-water interface before starting to attenuate. The transition stage exists, since for high energy photons, the photon radiation length is not considerably larger than the maximum secondary electron range (e.g. for 10 MeV photons: $\lambda = 25$ cm, $R = 5$ cm, and $\lambda/R \approx 5$) [49]. However, at depths greater than R, the ratio G_l/G_d remains constant, forming a transient charged particle equilibrium stage (TCPE).

2.2.3 The theorems of Fano and O'Connor

The dosimetric data used in the various dose calculation methods are mainly derived for water. However, the data can be transferred to other media with different
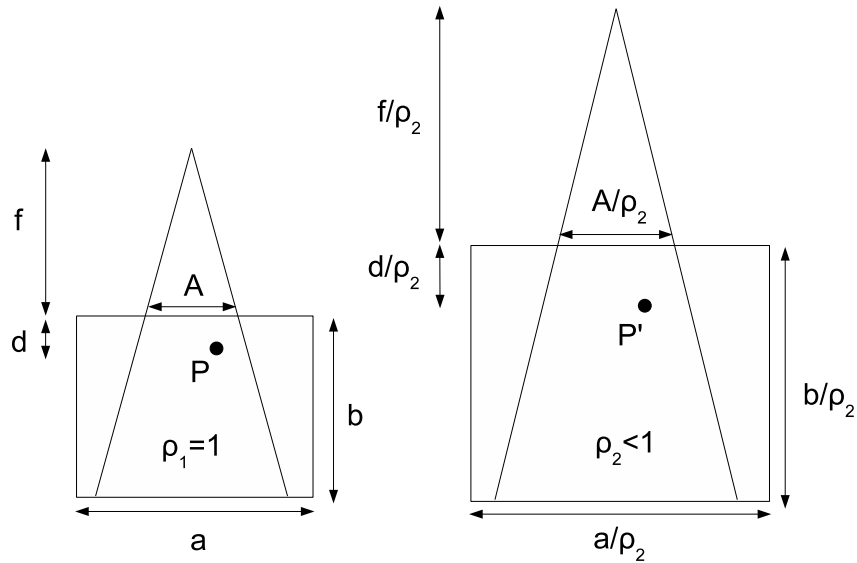
Fig. 5: The absorbed dose at points P and P' are same according to the theorem of O'Connor. All the linear dimensions in the right-hand side system have been scaled with the reciprocal of the material density, (modified from [50]).

density but identical atomic composition by applying the theorems of Fano and O'Connor [10]. The Fano's theorem states that in a radiation field with uniform fluence of primary particles (photons), the fluence of secondary particles (electrons) is independent of the density of the medium, as well as of the density variations from point to point [51]. Consequently, the absorbed dose along any line in the medium containing density variations would be constant. Fano's theorem assumes that the CPE conditions are fulfilled in both media across the density interface, which implies that the beam diameter must be large enough to realize a practical equilibrium. Fano's theorem is the basis of radiation dosimetry for ionization chambers.

The theorem of O'Connor states that the absorbed dose in corresponding points in two systems consisting of materials with different density, but of equal atomic composition, are the same provided that all linear dimensions are scaled by the reciprocal of the density [50]. This means that e.g. the dimensions of the phantom, field size in both directions, and SSD must be scaled by $1/\rho$ (see Fig. 5). In this context, the term density is related to the number of interaction centers per unit volume [25], which can be approximated by the electron density (ρ_{el}) in photon beam irradiation in the energy range where Compton interactions dominate [52].

Both theorems presented above are based on a common assumption that the interaction cross-sections of primary and secondary radiation per unit mass are independent of the density of the medium. Fano's theorem is applicable to CPE situations in a medium with density variations, while O'Connor's theorem relates the dose in two media with different density to each other. The theorem of O'Connor does not require CPE, although the fluence of primary particles at points P and P'

in Fig. 5 is the same due to the construction of the geometry. According to Fano's theorem, the fluence of secondary particles is the same, from which the equality of the doses follows. The density scaling of the kernels in superposition/convolution methods is one application of the O'Connor's theorem.

2.3   Measurement of absorbed dose

The ionization chamber is the most commonly used dosimeter for measuring the absorbed dose, which is due to the accuracy, instant readout, constant sensitivity over the detector lifespan, and good understanding of the necessary corrections [45]. Ion chamber has been used to provide measurement data in **II**, **III**, **IV** and **V**. Other common dosimeters include radiochromic and radiographic film, thermoluminescent devices, and semiconductor detectors such as diodes and diamond. The ionization chamber contains a sensitive volume filled with air, from which the ionization charge Q produced by the radiation in the sensitive air mass m_{air} is collected with a central electrode. The absorbed dose in air D_{air} is related to the ionization charge Q as [45]:

$$D_{\mathrm{air}} = \frac{Q}{m_{\mathrm{air}}} \left(\frac{W_{\mathrm{air}}}{e} \right), \tag{2.17}$$

where (W_{air}/e) is the mean energy required to produce an ion pair in air per unit charge (estimated value for dry air is 33.97 J/C). The dose in the surrounding medium (usually water) is obtained from D_{air} by applying either the Bragg-Gray or Spencer-Attix cavity theory.

The Bragg-Gray cavity theory is applicable for the situations where (a) the cavity is small in comparison with the range of charged particles striking it, so that the charged particle fluence of the medium is not disturbed, and (b) the absorbed dose to the cavity is deposited by the charged particles crossing it. The condition (a) is fulfilled only in the regions of CPE or TCPE. According to Bragg-Gray theory, the dose in the medium D_{med} is related to the dose in the cavity D_{cav} as [45]:

$$D_{\mathrm{med}} = D_{\mathrm{cav}} \left(\frac{\bar{S}_{\mathrm{col}}}{\rho} \right)_{\mathrm{med,cav}}, \tag{2.18}$$

where $(\bar{S}_{\mathrm{col}}/\rho)_{\mathrm{med,cav}}$ is the ratio of the average *unrestricted* mass collision stopping powers of the medium and the cavity. The linear stopping power S is the expectation value of energy loss per unit path length (dE/dx) by a charged particle, and the mass stopping power S/ρ is obtained by dividing the linear stopping power with the material density. The collision stopping power S_{col} accounts only for the interactions of the charged particles with the atomic orbital electrons.

The Spencer-Attix cavity theory also accounts for secondary (delta) electrons

created in the cavity during the slowing down of the primary electrons. There, the secondary electron fluence is divided into two components according to a user-defined cut-off energy Δ; secondary electrons having energy smaller than Δ are considered slow and are assumed to deposit their energy locally, and electrons with larger energy are considered fast. The Spencer-Attix relationship between D_{med} and D_{cav} is [45]:

$$D_{\text{med}} = D_{\text{cav}} \, s_{\text{med,cav}}, \qquad (2.19)$$

where $s_{\text{med,cav}}$ is the ratio of average *restricted* mass collision stopping powers (energy larger than Δ) of the medium and the cavity. Since the material of the ion chamber wall and central electrode are not equivalent to the surrounding medium, they can be accounted for as perturbations to the electron fluence of the medium in a following way [45]:

$$D_{\text{med}} = D_{\text{air}} \, s_{\text{med,air}} \, p_{\text{fl}} \, p_{\text{dis}} \, p_{\text{wall}} \, p_{\text{cel}}, \qquad (2.20)$$

where p_{fl} is a correction factor for electron fluence, p_{dis} is a correction factor for the displacement of the effective measurement point, p_{wall} is a wall correction factor, and p_{cel} is the correction factor for the central electrode. Eq. (2.20) is valid for thin-walled chambers, for which the wall thickness is much smaller than the range of secondary electrons. Thin-walled chambers are the most common chamber type at present [45].

Table 1: Experimental radiation quantities commonly used in photon dose calculation methods, (modified from [10] and [53]). Definition of the symbols used: D = detector response, A = field size at a certain distance from the source, d_{max} = depth of dose maximum, SSD = source-to-surface distance, SDD = source-to-detector distance.

Quantity	Definition
Percentage depth dose	$\text{PDD}(A_{\text{SSD}}; z) = \frac{D(A_{\text{SSD}}; z)}{D(A_{\text{SSD}}; d_{\text{max}})} \times 100$
Profile Off-axis ratio	$P_{\text{O}}(A_{\text{SSD}}; x, z) = \frac{D(A_{\text{SSD}}; x, z)}{D(A_{\text{SSD}}; x=0, z)} \times 100$
Diagonal profile	$P_{\text{D}}(A_{\text{SSD}}; r, z) = \frac{D(A_{\text{SSD}}; r, z)}{D(A_{\text{SSD}}; r=0, z)} \times 100$
Tissue-maximum ratio	$\text{TMR}(A_{\text{SDD}}; z) = \frac{D(A_{\text{SDD}}, \text{SDD}; z)}{D(A_{\text{SDD}}, \text{SDD}; z_{\text{dmax}})}$
Tissue-air ratio	$\text{TAR}(A_{\text{SDD}}; z) = \frac{D(A_{\text{SDD}}, \text{SDD}; z)}{D_{\text{build-up cap}}(A_{\text{SDD}}, \text{SDD})}$
Scatter-air ratio	$\text{SAR}(A_{\text{SDD}}; z) = \text{TAR}(A_{\text{SDD}}; z) - \text{TAR}(0; z)$
Total scatter factor Output factor	$S_{c,p}(A) = \frac{D(A; z_{\text{cal}})}{D(A_{\text{cal}}; z_{\text{cal}})}$
Collimator scatter factor	$S_c(A) = \frac{D_{\text{mini-phantom}}(A; z_{\text{cal}})}{D_{\text{mini-phantom}}(A_{\text{cal}}; z_{\text{cal}})}$
Phantom scatter factor	$S_p(A) = S_{c,p}(A)/S_c(A)$

Basic measurement-based quantities that are commonly used in dose calculation methods are presented in Table 1. When measuring PDDs or profiles in water, the SSD is fixed, and the detector is moved in the phantom along a straight line during irradiation. In the PDD measurement, the detector is moved along the central axis (CAX) of the beam, usually starting from the largest depth towards the surface to avoid artifacts resulting from disturbed water surface. Profiles are measured in a plane perpendicular to the PDD, along the collimator axes in x- and y-direction. When measuring the diagonal profiles, the detector is moving along the field diagonal i.e. from one corner of the field through the center of the field towards the other corner.

In TAR measurement, the source-to-detector distance (SDD) is kept fixed, and the amount of water above the detector is varied during the measurement. This results in a depth-dependent curve, which is normalized by the measurement in air using the same geometry. In order to reach the CPE in air, a build-up cap made of a relatively high-density material is attached to the detector.

Total scatter factors (output factors) $S_{c,p}(A)$ are measured with constant SSD and SDD, and the detector is located at a certain calibration depth z_{cal} in a phantom. The detector reading per monitor units (MUs) is recorded as a function of field size A, whereafter it is normalized to the reading of a calibration field size A_{cal}. The measurement of the collimator scatter factor $S_c(A)$ is similar, with the exception that the detector is placed in a narrow cylindrical miniphantom with a diameter of ∼4 cm [54]. The axis of the miniphantom must coincide with the beam axis. The response of the detector in the mini-phantom is proportional to the beam energy fluence Ψ in air provided that the whole volume of the mini-phantom is irradiated [55].

3 Dose calculation methods

Some methods for absorbed dose calculations in the patient are described in this chapter. First, the semi-empirical PBC method is presented, since it used as a reference method in **III**. This is followed by the description of methods to account for heterogeneous patient tissues that are used with empirical dose calculation methods. Finally, the kernel-based dose calculation method, originally described in **I**, is presented.

3.1 Pencil Beam Convolution (PBC) algorithm

3.1.1 Dose computation using the pencil-beam kernel

In PBC, the dose for an irregular field F is obtained by convolving a field intensity distribution with a pencil-beam kernel, which has been derived from the measured beam data. The dose computation can be expressed analytically as [13]:

$$D(x, y, z; F) = \frac{(f + z_{\mathrm{ref}})^2}{(f + z)^2} \int_{-\infty}^{\infty} \int_{-\infty}^{\infty} F(u, v) P_{\mathrm{int}}(u, v, z) K(x - u, y - v, z) \, \mathrm{d}u \mathrm{d}v, \quad (3.1)$$

where f is the SSD, $F(x, y)$ the field intensity function, $P_{\mathrm{int}}(x, y, z)$ the intensity profile, and $K(x, y, z)$ the pencil-beam kernel, and z_{ref} the reference depth used for normalization. The function $F(x, y)$ describes field blocking; it is unity for points inside the field opening, and zero or a user-given transmission factor through the beam limiting devices (e.g. MLC) outside the field. The intensity profile $P_{\mathrm{int}}(x, y, z)$ accounts for the variation of the primary photon fluence as a function of off-axis distance and depth. The pencil-beam kernel $K(x, y, z)$ describes the dose distribution of a very narrow beam entering a water phantom along the z-axis. The functions $P_{\mathrm{int}}(x, y, z)$ and $K(x, y, z)$ in Eq. (3.1) are derived from the measured beam data of several square field sizes.

The convolution in Eq. (3.1) is performed only at five standard depths to reduce computation time, whereas the dose for other depths interpolated. In order to enable accurate interpolation, the dose at an arbitrary depth z is computed as [53]:

$$D(x, y, z; F) = D_a(z; F) P(x, y, z; F), \quad (3.2)$$

where $D_a(z; F)$ is the PDD along the effective field axis and $P(x, y, z; F)$ the off-axis ratio. $D_a(z; F)$ is computed as a product of the measured PDD for an effective square field size A, and the correction factor, which accounts for the difference in the PDD between the irregular field F and the effective field A. The correction factor is directly computed for five standard depths, whereas for other depths it is linearly interpolated. The off-axis ratio $P(x, y, z; F)$ can be directly computed at

the five standard depths as the ratio of doses at an arbitrary position (x, y) and at the effective field central axis [53]. For the other depths, $P(x, y, z; F)$ is linearly interpolation along the fanlines.

3.1.2 Derivation of the pencil-beam kernel and the intensity profile from measurements

For the computation of the pencil-beam kernel $K(x, y, z)$ and the intensity profile $P_{\text{int}}(x, y, z)$, the measured profile P_{O} is divided into a boundary profile P_b and an envelope profile P_c [56]:

$$P_{\text{O}}(x, z; X) = P_c(x, z)P_b(x, z; X), \tag{3.3}$$

where X is the size of the square field. The envelope profile P_c describes the change in the absorbed dose as a function of off-axis distance, and it is basically computed by averaging the measured profiles at each off-axis position. The boundary profile P_b describes either the field boundary, or, far enough from the boundary region, the total contribution of transmission through the beam limiting devices.

In addition to this, intermediate concepts of scatter kernel K_s and boundary kernel K_b presented in [12] are required for deriving $K(x, y, z)$ and $P_{\text{int}}(x, y, z)$. Due to its cylindrical symmetry, the pencil-beam kernel $K(x, y, z)$ can be denoted as $K(r, z)$. The integral of $K_s(r, z)$ multiplied by $P_{\text{int}}(r, z)$ along a circular disk with a radius of R yields to a scatter dose $D_{\text{scat}}(z; R)$. This quantity can be derived from the measurements of an equivalent square field X as a product of the depth dose $\text{PDD}(z; X)$ and the phantom scatter factor $S_{\text{p}}(X)$. By using $D_{\text{scat}}(z; R)$ derived from the measurements for several values of R, and approximating P_{int} with P_c, the values of $K_s(r, z)$ at different radii can be derived via numerical differentiation. The scatter kernel K_s and the intensity profile P_{int} are defined such that their convolution equals the envelope profile P_c. Hence, an improved estimate of P_{int} can be derived using an iterative procedure for the convolution equation. The scatter kernel K_s is then re-computed by utilizing the information about P_{int} in the computation instead of the initially used P_c. If the resulting K_s would now be substituted by K in Eq. (3.1), the calculated profiles would have unrealistic, too sharp penumbra. To correct this phenomenon, the concept of the boundary kernel K_b is needed.

The boundary kernel K_b is derived from the boundary profile P_b' that has been corrected for photon scatter. This is done in order to remove the effect of the already determined part of the pencil-beam kernel from the profiles. It is then assumed that this modified boundary profile is the convolution of the boundary kernel K_b with a uniform square field (1 inside the field, 0 outside). The boundary kernel K_b is then derived in a two-phase process from the corrected boundary profile P_b' [12, 13]. Finally, the scatter and boundary kernels are combined into a single pencil-beam

kernel $K(r, z)$ to be used in Eq. (3.1) by using the rules presented in [13].

As a summary, the pencil-beam kernel $K(x, y, z)$ and the intensity profile $P_{\text{int}}(x, y, z)$ are derived from the measured depth dose curves $\text{PDD}(z; X)$ for several square field sizes ranging from 4×4 to 40×40 cm^2, the measured profiles $P_O(x, z; X)$ at five standard depths for the same field sizes, the diagonal profiles for the largest field size (used in computation of P_c) and from the phantom scatter factors $S_p(X)$ obtained from the table in [57]. These quantities are then used to compute the dose distribution at five reference planes according to Eq. (3.1), while the dose at the other depths is obtained via interpolation.

3.1.3 Extension of the method to the actual patient geometry

In a real patient geometry, where e.g. the SSD may differ from the SSD used in the basic set of beam data measurements, some additional correction factors are needed. In this case, the dose at an arbitrary point (x, y, z) for field F is computed as [53]:

$$D(x, y, z; F) = DD(z; F)P(x, y, z; F)\, C_O\, C_{\text{inh}}, \tag{3.4}$$

where $DD(z; F)$ is the PDD at the SSD of the patient geometry, $P(x, y, z)$ the off-axis ratio, C_O the correction factor for oblique skin, and C_{inh} the correction factor for tissue inhomogeneities. The PDD component $DD(z; F)$ is defined as [53]:

$$DD(z; F) = D_a(z; F)C_{MF}(z), \tag{3.5}$$

where D_a is the PDD defined in Eq. (3.2), and the factor $C_{MF}(z)$ considers the change of SSD from f_1 (used in basic beam data measurements) to f_2 (patient geometry) as [53]:

$$C_{MF}(z) = \frac{\text{TAR}(z; A_2)}{\text{TAR}(z; A_1)} \left(\frac{f_1 + z}{f_2 + z}\right)^2 \left(\frac{f_2 + d_{\max}}{f_1 + d_{\max}}\right)^2, \tag{3.6}$$

where A_i $(i = 1, 2)$ is the equivalent field size defined at depth z with SSD of f_i and $d_{\max}$ is the depth of dose maximum. The largest effect in Eq. (3.6) is caused by the inverse-square law correction, whereas the TAR ratio is a second-order correction for the changes in scatter dose. The correction factor for oblique skin C_O takes into account the effect of non-flat patient surface on the total dose in a similar principle as in Eq. (3.6) for each fanline. For the computation of the inhomogeneity correction factor C_{inh}, PBC algorithm has several options, which will be discussed later in Sec. 3.2.

The PBC algorithm descibed here is much more sophisticated than the other empirical methods (e.g. Cunningham-Clarkson integration) and it provides a large improvement over the earlier two-pencil-beam algorithm [12]. Nevertheless, one ma-

jor limitation of the method is that the extra-focal radiation is not modeled, leading to deviations exceeding 2% in the regions outside the field edge. Since correction factors are required to model the actual patient geometry, the calculation accuracy in realistic patient cases is expected to be poorer than that of more sophisticated methods (superposition/convolution methods or MC). In addition, tissue heterogeneities cannot be inherently taken into account in the dose calculation, forcing the method to rely on the correction factor techniques. Another drawback is that the calculated pencil-beam is directly influenced by the methods and equipment that are used to specify of the basic set of beam data.

3.2 Correction factor based methods to account for tissue heterogeneities

Empirical and semi-empirical dose calculation methods generally assume that the patient tissue is water-equivalent. Therefore, correction factors are required in more realistic cases, where the calculation volume consists of heterogeneous tissue components. Both the primary and the scattered components of a radiation beam are possibly affected by a heterogeneity in the irradiated volume. The primary radiation at an arbitrary point P consists of photons, which have not interacted anywhere in the medium before reaching the point P. The scattered radiation, on the other hand, is composed of photons that have experienced one or more interactions on their path to the point P. The effect on the primary component is dependent only on the thickness of the heterogeneity on the radiation path, whereas the scatter component is also affected by the position and lateral dimensions of the heterogeneity. Often the changes on primary and scatter components result in effects in the opposite directions. For example, a low-density slab-like heterogeneity will decrease the attenuation of the primary radiation, and thus the dose at a point within the heterogeneity increases. On the other hand, the mass of the scattering material decreases, resulting in a decrease in the scattered radiation component at the same point. In most cases, the effect of heterogeneity is larger on the primary than on the scattered component [52].

3.2.1 Primary beam effective pathlength methods

The simplest methods, such as the effective attenuation coefficient method, correct only for the changes in the primary radiation component. These methods utilize the concept of effective (radiological) thickness d_{eff}, which is defined as [10]:

$$d_{\text{eff}} = \frac{1}{\rho_{\text{water}}} \int_0^d \rho(z) \, \mathrm{d}z, \tag{3.7}$$
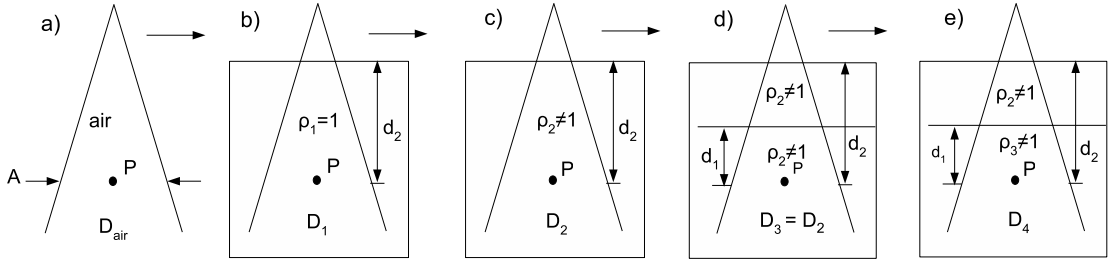
41

Fig. 6: Derivation for the Batho power law for a point positioned under a single hetero-geneity layer but within non-water-equivalent material, (modified from [52]).

where d is the geometrical depth, $\rho(z)$ the density at depth z, and ρ_{water} the density of water. The densities in Eq. (3.7) are usually estimated from the CT image. The depth-dependent correction factor $\text{CF}(d)$ for the effective attenuation coefficient method can be written as [10]:

$$\text{CF}(d) = e^{-\mu_{\text{w}}(d_{\text{eff}}-d)}, \tag{3.8}$$

where μ_{w} is the linear attenuation coefficient for water (estimated from the PDD data). The methods that take into account only the changes in the primary component, are capable of clinically acceptable accuracy provided that the calculation point is sufficiently far from the heterogeneity. In this case, the scatter from the heterogeneity is not able to reach the calculation point. However, close to the heterogeneity errors as large as 10% may occur in certain geometries [52].

3.2.2 Batho power law method

The method suggested by Batho [14] partially accounts also for the change in the scattering volume by utilizing the tissue-air ratios raised to a power. The method was originally presented as an empirical correction for a calculation point located in tissue-equivalent material below a lung-type heterogeneity for Co-60 irradiation. This formalism was later generalized by Sontag and Cunningham [52] to a situation, where the calculation point may be situated within a heterogeneity or below it. Later, the Batho power law was extended to handle multiple regions of slab-like heterogeneities.

The generalized Batho power law can be derived by analyzing a few simple geometries (see Fig. 6) [52]. The absorbed dose at point P in air resulting from the irradiation of field size A is denoted by D_{air} as shown in Fig. 6(a). Furthermore, the dose D_1 at the same point in a homogeneous water phantom at a depth d_2, as shown in Fig. 6(b), is related to the dose in air as [52]:

$$D_1 = D_{\text{air}}\text{TAR}(A; d_2), \tag{3.9}$$

which follows directly from the definition of the TAR. Hence, $\mathrm{TAR}(A; d_2)$ describes the factor by which the dose in air must be modified to obtain the dose in water. If the density of the medium would be changed from 1.0 to 2.0, the number of atoms and electrons, and thus also the interactions would be doubled. Therefore, to obtain the dose D_2 at the same point in the phantom with density 2.0, the modifying factor would have to be applied twice in a multiplicative way. Even though this is not true in an absolute sense, it is a good approximation [52]. For a heterogeneity with an arbitrary density ρ_2, the dose at point P in Fig. 6(c) is therefore [52]:

$$D_2 = D_{\mathrm{air}} \mathrm{TAR}(A; d_2)^{\rho_2}. \tag{3.10}$$

Based on the Eqs. (3.9)-(3.10), the ratio of the doses in water and in medium with density ρ_2 can we written as [52]:

$$D_2/D_1 = \mathrm{TAR}(A; d_2)^{\rho_2}/\mathrm{TAR}(A; d_2). \tag{3.11}$$

Let us next consider a situation in Fig. 6(d), where the previous geometry is changed such that there is an additional boundary at a distance $d_1 < d_2$ above the point P, while keeping the material densities unchanged. Since the situation is identical to Fig. 6(c), D_3 equals D_2. If the density below the boundary is then changed to ρ_3 as in Fig. 6(e), the ratio of doses D_4 and D_3 can be obtained in an analogous way to the ratio D_2/D_1 [52]:

$$D_4/D_3 = \mathrm{TAR}(A; d_1)^{\rho_3}/\mathrm{TAR}(A; d_1)^{\rho_2}. \tag{3.12}$$

The overall correction factor CF, such that $D_4 = \mathrm{CF} \cdot D_1$, can be derived from Eqs. (3.11)-(3.12) [52]:

$$\mathrm{CF} = \frac{\mathrm{TAR}(A; d_1)^{\rho_3 - \rho_2}}{\mathrm{TAR}(A; d_2)^{1 - \rho_2}} \frac{(\mu_{\mathrm{en}}/\rho)_{\rho_3}}{(\mu_{\mathrm{en}}/\rho)_{\rho_2}}, \tag{3.13}$$

which applies for a point P located at depth d_1 below the surface of material with density ρ_3, and where ρ_2 is the density of the overlying material with thickness $d_2 - d_1$. Eq. (3.13) includes as an additional term the ratio of the mass energy absorption coefficients, which accounts for the dependence from the atomic number for certain interactions.

The generalized Batho power law presented in Eq. (3.13) is based on the following assumptions [52]:

1. Only the material above the calculation point P is considered in the calculation of the correction factor. It is assumed that the material below P is the same as that of the point P.

2. The effect of a heterogeneity on the dose is assumed to be independent of the thickness of the tissue-equivalent material located above the heterogeneity.

3. CPE exists at the point of interest.

4. The lateral dimensions of all regions are assumed to be at least as large as the beam dimensions.

For high-energy radiation at locations near the heterogeneity interface, the assumption (3) is disturbed, and may lead to considerable errors. The last assumption limits the use of the Batho correction for heterogeneities with small dimensions with respect to the field size.

It was later shown that the correction factor should rather be based on the tissue-maximum ratios (TMRs) shifted by the build-up depth than on the initially proposed TARs [58, 59]. The use of TMR instead of TAR improves the accuracy of the correction inside low-density heterogeneity especially for large field sizes [58]. The modification of the depth with the build-up depth enables the use of TMR for cases, where the distance from the heterogeneity interface to the calculation point is smaller than the build-up depth. In addition, the accuracy in high-energy beams is significantly improved [59]. Multiple heterogeneity layers can be accounted for by dividing the material along the beam up to certain depth into several layers, each approximated with single density value. The total correction factor is obtained by multiplying the individual correction factors for each layer. The following generalized formulation is also used as the modified Batho power law correction in the PBC algorithm [10]:

$$\mathrm{CF}(z) = \frac{(\mu_{\mathrm{en}}/\rho)_N}{(\mu_{\mathrm{en}}/\rho)_{\mathrm{w}}} \prod_{m=1}^{N} \left(\mathrm{TMR}(z - z_m + z_{\mathrm{bu}})\right)^{(\mu_m - \mu_{m-1})/\mu_{\mathrm{w}}}, \qquad (3.14)$$

where $(\mu_{\mathrm{en}}/\rho)_N$ and $(\mu_{\mathrm{en}}/\rho)_{\mathrm{w}}$ are the mass energy absorption coefficients for layer N and water, respectively; z_m the distance along the beam from the surface to layer m, z_{bu} the build-up depth, and μ_m the linear attenuation coefficient for layer m.

3.3 Dose calculation method based on the superposition of Monte Carlo simulated pencil-beams

In this section, the dose calculation method developd in this thesis is presented. Although both PBC and the method originally described in **I** utilize pencil-beam kernels, the former method derives the kernel directly from measurements, whereas in the latter method, the kernel is obtained by weighting MC simulated kernels with the beam spectrum. The characterization of the fluence and the spectrum of radiation beam is obtained from the beam model described in **II**. Due to more physics-based approach to the dose computation problem, the developed method
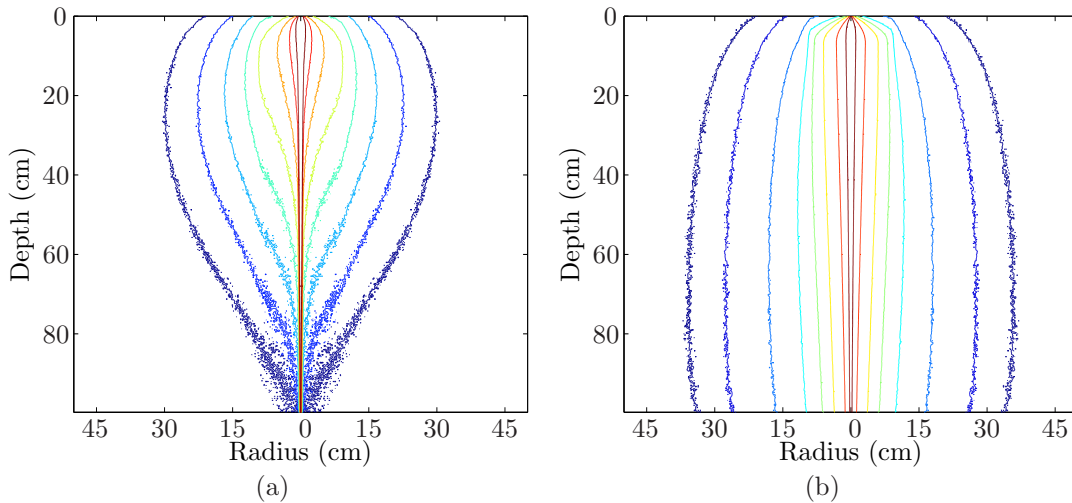
Fig. 7: MC simulated pencil-beam kernels $h_E(r, z)$ of monoenergetic photons for (a) $E = 1\ MeV$ and (b) $E = 15\ MeV$. The contours are shown in the base-10 logarithmic scale at the levels [-45,...,-38] in (a) and at the levels [-45, -44, -42.5, -41, -39.5, -38, -36, -34] in (b). The kernel $h_E(r, z)$ is expressed in grays per incident particle fluence.

is directly applicable to irregular beam shapes, variable SSDs and oblique patient surfaces. The use of pencil-beam kernels instead of point-spread kernels gives a significant speed advantage. However, when using the pencil-beams, the effect of patient heterogeneities on the dose distribution cannot be fully taken into account in 3D. On the other hand, the mechanism developed for modeling tissue heterogeneities has been shown to result in acceptable accuracy for most clinical situations, and to provide significant improvement over the conventional Batho power law correction commonly used in PBC [**I**, **III**].

3.3.1 Modeling of the pencil-beam

The pencil-beam represents the energy deposition of an infinitesimally narrow photon beam incident on a semi-infinite water phantom. In this work, pencil-beams $h_E(r, z)$ were pre-calculated for monoenergetic photons in the energy range $E = 0.25, \ldots, 25$ MeV using the EGSnrc MC code [27] with a constant number of particle histories for each energy. The MC simulated pencil-beam kernels for the energies of 1 and 15 MeV are visualized in Fig. 7. Due to cylindrical symmetry of dose deposition about the z-axis, it is possible to reduce the computation time using cylindrical scoring geometry. The EGSnrc-simulated kernels $h_E(r, z)$ are expressed in units of dose per incident particle fluence [Gy $\cdot$ cm^2], but for further processing the kernels are divided by the energy E of the pencil-beam and multiplied by the mass density of water. The modified kernel is denoted as $h'_E(r, z)$ [1/m$^3 \cdot$ cm^2], the volume integral of which is constant for each E. This normalization enables the dose calculations to be performed in absolute units, so that the MUs can be directly determined from the calculated dose distribution.

45

The broad beam produced by the treatment unit is divided into beamlets, whose cross-section at the isocenter plane is a square with a side length Δ, which is user-definable parameter in the range $0.1, \ldots, 0.5$ cm. Dose deposition in the patient can be viewed as a superposition of the dose contributions of individual beamlets weighted by the spatially varying energy fluence. The polyenergetic pencil-beam representing beamlet β is constructed as:

$$h_\beta(r, z) = \int h'_E(r, z) \Psi_{E,\beta}(E) \, dE / \int \Psi_{E,\beta}(E) \, dE, \qquad (3.15)$$

where $\Psi_{E,\beta}$ is the energy fluence spectrum for primary photons in air for beamlet β, which here describes only the distribution of beamlet energy into different energy bins. The total amount of energy carried by the beamlet is modeled with the energy fluence parameter Ψ_β, see Eq. (3.26). In most prior kernel-based methods, such as in [20, 21], the effect of the off-axis spectrum variations on the kernel shape is not directly taken into account, but some more or less heuristic correction factors are used instead.

In the method developed here, the energy deposition computations are performed in a diverging coordinate system. This is beneficial, since all rays originating from the target, which is assumed to be a point source, have constant x- and y-coordinates in the calculation grid. This makes it straightforward to perform calculations with oblique pencil-beam kernels. A mapping $\mathcal{M} : \mathbf{x} \mapsto \mathbf{p}$ from the orthogonal to the diverging coordinate system is defined as:

$$\mathcal{M}(\mathbf{x}) = \left(\frac{d_{\mathrm{SAD}}}{x_z} x_x, \frac{d_{\mathrm{SAD}}}{x_z} x_y, \sqrt{x_x^2 + x_y^2 + x_z^2} \right), \qquad (3.16)$$

where d_{SAD} is the source-to-axis distance, $\mathbf{x} = (x_x, x_y, x_z)$ is a vector in the orthogonal coordinate system and $\mathbf{p} = (p_x, p_y, p_z)$ is the corresponding vector in the diverging coordinate system. After the pencil-beams $h_\beta(r, z)$ have been transferred into the diverging coordinate system as described in $\mathbf{I}$, the cylindrical symmetry is no longer valid, and hence the pencil-beam is be subscripted with three coordinates $\mathbf{p} = (p_x, p_y, p_z)$.

The pencil-beam representing a beamlet is then divided into depth-directed and lateral components in order to facilitate the correction for tissue heterogeneities along both of these directions separately. This is a crucial approximation of the method, but it affects the calculation accuracy only in heterogeneous cases. The depth-directed component $\tilde{I}_\beta$ can be defined as an integral of the pencil-beam over the calculation plane [60]:

$$\tilde{I}_\beta(p_z) = \iint h_\beta(s, t, p_z) \, ds \, dt. \qquad (3.17)$$
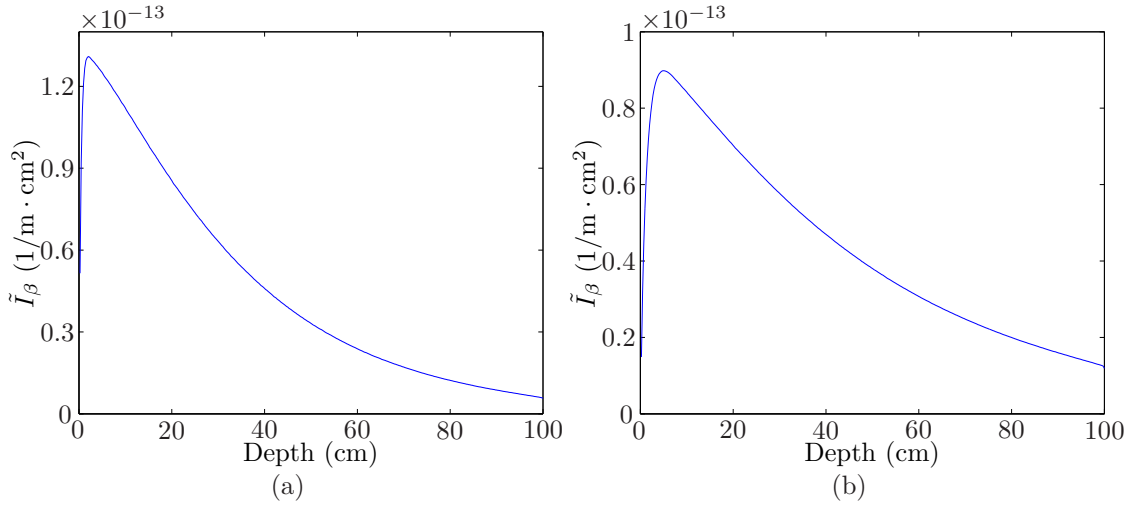
Fig. 8: The depth-directed component $\tilde{I}_\beta(p_z)$ for (a) 6 MV and (b) 18 MV photon beams at the CAX.

The function of Eq. (3.17) describes the distribution of the energy deposited by beamlet β along the depth direction. Examples of $\tilde{I}_\beta(p_z)$ at the CAX for 6 and 18 MV beams are shown in Fig. 8. The lateral component f_β of the pencil-beam having CAX at (p_x, p_y) can be defined as:

$$f_\beta(\theta, \lambda, p_z) = h_\beta(p_x + \lambda \cos\theta, p_y + \lambda \sin\theta, p_z)/\tilde{I}_\beta(p_z), \qquad (3.18)$$

which represents the fraction of energy (per unit area) deposited onto an infinitesimally small angular sector $d\theta$ at distance λ from the pencil-beam CAX. The lateral component is slightly different for each angle θ around the CAX of the pencil-beam, since cylindrical symmetry is not valid in the diverging coordinate system. By definition, the original pencil-beam h_β with CAX at (p_x, p_y) can be reconstructed from the individual components as:

$$h_\beta(x, y, p_z) = \tilde{I}_\beta(p_z)f_\beta(\theta, \lambda, p_z), \qquad (3.19)$$

where $\lambda = \sqrt{(x - p_x)^2 + (y - p_y)^2}$ and $\theta = \arctan[(y - p_y)/(x - p_x)]$.

3.3.2 Exponential fitting of the lateral component

The lateral component f_β is modeled as a sum of radial exponential functions:

$$k_\beta(\theta, \lambda, p_z) = \frac{1}{\lambda} \sum_{i=1}^{N} c_i(\theta, p_z)e^{-\mu_i \lambda}, \qquad (3.20)$$

where the same pre-selected attenuation coefficients μ_i are used for each θ and p_z to allow efficient computer implementation. The weight parameters $c_i(\theta, p_z)$ are

47

optimized such that the difference between f_β and k_β is minimized. This analytical modeling is performed, since the use of exponential functions enables efficient computation of scatter on each calculation plane (see Sec. 3.3.6). The value of $N = 6$ has been used in Eq. (3.20) to obtain a good approximation of f_β while still achieving relatively high computational efficiency. The effective ranges $1/\mu_i$ of [1, 2.5, 6, 15, 40, 100] mm have been used in the algorithm. The fitting is performed in terms of the integral functions over an angular sector $[\theta_j, \theta_{j+1}]$, where $\theta_{j+1} - \theta_j = \pi/8$, up to a maximum radius of λ:

$$F_\beta(\theta, \lambda, p_z) = \int_{t=\theta_j}^{\theta_{j+1}} \int_{u=0}^{\lambda} f_\beta(t, u, p_z) \, \mathrm{d}t \, u \mathrm{d}u \tag{3.21}$$

$$K_\beta(\theta, \lambda, p_z) = \int_{t=\theta_j}^{\theta_{j+1}} \int_{u=0}^{\lambda} k_\beta(t, u, p_z) \, \mathrm{d}t \, u \mathrm{d}u, \tag{3.22}$$

such that K_β is fitted to F_β. The integral transform in Eqs. (3.21)-(3.22) is used, since it penalizes for consecutive fitting errors of the same sign, and accounts for the fact that kernel values with larger radius are deposited over larger areas creating a model that is accurate over a wide range of field sizes. The function K_β in Eq. (3.22) can be written as:

$$K_\beta(\theta, \lambda, p_z) = \sum_{i=1}^{N} \int_{t=\theta_j}^{\theta_{j+1}} \int_{u=0}^{\lambda} \frac{1}{u} c_i(\theta, p_z) e^{-\mu_i u} \, \mathrm{d}t \, u \mathrm{d}u = \sum_{i=1}^{N} \tilde{c}_i(\theta, p_z)(1 - e^{\mu_i \lambda}), \tag{3.23}$$

where $\tilde{c}_i = \pi c_i/(8\mu_i)$ and $\sum_{i=1}^{N} \tilde{c}_i = 1$. Thus, the fitting problem for a fixed angular sector and depth can be written in a matrix notation as:

$$\underbrace{\begin{bmatrix} 1 - e^{-\mu_1 \lambda_0} & \cdots & 1 - e^{-\mu_N \lambda_0} \\ \vdots & \ddots & \\ 1 - e^{-\mu_1 \lambda_m} & & 1 - e^{-\mu_N \lambda_m} \end{bmatrix}}_{\mathbf{A}} \underbrace{\begin{bmatrix} \tilde{c}_1 \\ \vdots \\ \tilde{c}_N \end{bmatrix}}_{\mathbf{x}} = \underbrace{\begin{bmatrix} F_\beta(\lambda_0) \\ \vdots \\ F_\beta(\lambda_m) \end{bmatrix}}_{\mathbf{b}}, \tag{3.24}$$

where $\lambda_0, \ldots, \lambda_m$ are the discrete values of λ, $\mathbf{A}$ the matrix of size $m \times N$, $\mathbf{x}$ the vector of size $N \times 1$, and $\mathbf{b}$ the vector of size $m \times 1$. The system of linear equations presented in Eq. (3.24) is overdetermined, since there exist m equations and N variables such that $m \gg N$. The least-squares solution minimizing the error $\|\mathbf{A}\mathbf{x} - \mathbf{b}\|$ is found by solving:

$$\mathbf{A}^\mathrm{T} \mathbf{A} \mathbf{x} = \mathbf{A}^\mathrm{T} b. \tag{3.25}$$

The LU-decomposition, where L and U refer to lower and upper triangular matrices, is a standard technique for solving linear equations [61]. This method has been used
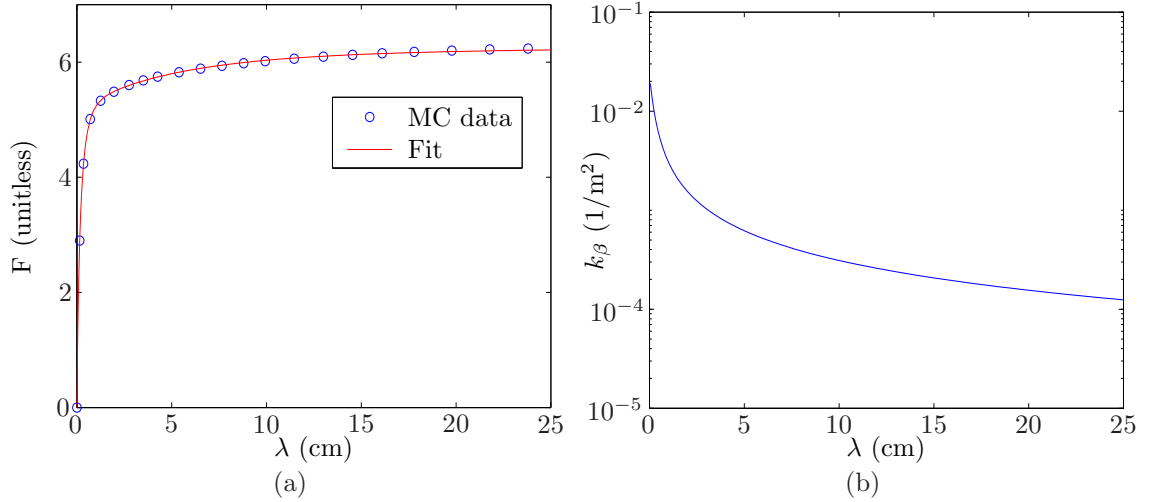
Fig. 9: (a) The result of the fit of $K_\beta(\theta, \lambda, p_z)$ to the MC simulated data $F_\beta(\theta, \lambda, p_z)$ for a 6 MV beam at CAX for an angular sector $\theta = [0, \ldots, \pi/8]$ and $p_z = 5$ cm. (b) Visualization of the resulting lateral scatter kernel $k_\beta(\theta, \lambda, p_z)$.

to solve Eq. (3.25), since it is numerically more stable than Gaussian elimination, and provides speed advantage because only the right-hand size of Eq. (3.25) changes for different angular sector and depth. An example of the fitting process and the resulting lateral scatter kernel is presented in Fig. 9.

To obtain the energy deposited by the beamlet β into a calculation point $\mathbf{p}$, we compute first the total energy to be released into the calculation layer from β:

$$I_\beta(p_z) = \Delta x \Delta y \, \Psi_\beta \int_{s=p_z-\Delta z}^{p_z} \tilde{I}_\beta(s) \, \mathrm{d}s, \qquad (3.26)$$

where Δx, Δy and Δz are the calculation resolutions in the three orthogonal directions, and Ψ_β is the energy fluence [J/m^2] for a beamlet β. Ψ_β is a constant in the diverging coordinate system, since the area of the grid element increases with depth according to the inverse-square law. Then, the fraction of energy deposited by a beamlet β into a calculation point $\mathbf{p}$ in the plane p_z is obtained as:

$$E_\beta(\mathbf{p}) = I_\beta(p_z)k_\beta(\theta, \lambda, p_z), \qquad (3.27)$$

which gives the deposited energy per unit area. The total energy deposited into a point $\mathbf{p}$ is obtained as a superposition of the contributions of all the beamlets comprising the broad beam:

$$E_{\text{total}}(\mathbf{p}) = \iint_\beta E_\beta(\mathbf{p}) \, \mathrm{d}\beta, \qquad (3.28)$$

where $\mathrm{d}\beta$ is the area of the beamlet cross-section projected to isocenter plane.

49

In addition to the photons originating from the point-like target, also the contributions of extra-focal photons scattered from the treatment head components and the contamination electrons are taken into account, as is described in **I**. The calculation of these components is similar to that of the primary photons, except that for extra-focal photons, the spectrum is assumed to be spatially invariant. In addition, the lateral component is approximated with that of the primary photons. In the calculation of the electron contamination contribution, the scattering occurring in the phantom (patient) is not explicitly modeled, but is assumed to be included in the fluence. Finally, both of these components are added to the total energy distribution of Eq. (3.28).

3.3.3   Extension of the method to heterogeneous cases

The method presented above is extended for heterogeneous tissues by utilizing the theorem of O'Connor (see Sec. 2.2.3) such that each spatial dimension is locally scaled by the reciprocal of the electron density relative to water (ρ_w). However, a further assumption is made that the density scaling can be performed independently for the depth-directed and lateral components. This is equivalent to the assumption that the particles would first travel to the destination plane along the beamlet CAX and then would be transported to the destination location along the spherical cell. This approach is similar to the rectilinear scaling utilized in the point-spread function methods, where the kernel is usually scaled according to the mean electron density between the primary interaction and the dose deposition sites [20]. The rectilinear scaling assumes that the particles imparting energy follow the same rectilinear path, which ignores the dose deposited by the multiple scattered particles. Keall and Hoban [62] have proposed an improvement to the rectilinear scaling. Their method accounts for the full density distribution between the interaction and deposition sites, but requires a three-fold calculation time compared to the more common approach. Although the assumptions made here may limit the calculation accuracy in certain situations, the presented method still results in better agreement with MC simulations in heterogeneous cases than another widely used pencil-beam based algorithm [21].

The depth-directed component in a general heterogeneous case can thus be defined as:

$$I'_\beta(p_z) = I_\beta(p'_z)\rho_\mathrm{w}(\mathbf{p}_\beta), \tag{3.29}$$

where p'_z is the radiological depth calculated as in Eq. (3.7) based on electron density information obtained from the CT-image, and $\mathbf{p}_\beta$ is the point on the pencil-beam CAX at depth p_z. The use of radiological depth in Eq. (3.29) inherently takes into account curved patient surface. Hence, a separate correction factor for oblique skin as in PBC in Eq. (3.4) is not needed. In a similar fashion, the lateral component k_β

in the heterogeneous case can be defined as:

$$k'_\beta(\theta, \lambda, p_z) = k_\beta \left(\theta, \frac{p'_z}{p_z}\lambda', p'_z \right) \rho_{\mathrm{w}}(\mathbf{p}), \tag{3.30}$$

where λ' is the radiological distance from the pencil-beam center point $\mathbf{p}_\beta$ to the calculation point $\mathbf{p}$ along the spherical shell. Since the lateral kernel values are taken from the radiological depth p'_z, it is necessary to scale the effective radius λ' by the ratio p'_z/p_z to correct for the diverging coordinate system. The multiplication with the relative electron density ρ_{w} in Eqs. (3.29)-(3.30) follows from the change of variables from the effective coordinates to the geometrical coordinates. An example of the scaled I- and k-functions in case of a cylindrical lung insert is shown in Fig. 10. The heterogeneity corrected energy distribution from a single beamlet β into a calculation point $\mathbf{p}$ is then calculated as:

$$E'_\beta(\mathbf{p}) = I'_\beta(p_z)k'_\beta(\theta, \lambda, p_z). \tag{3.31}$$
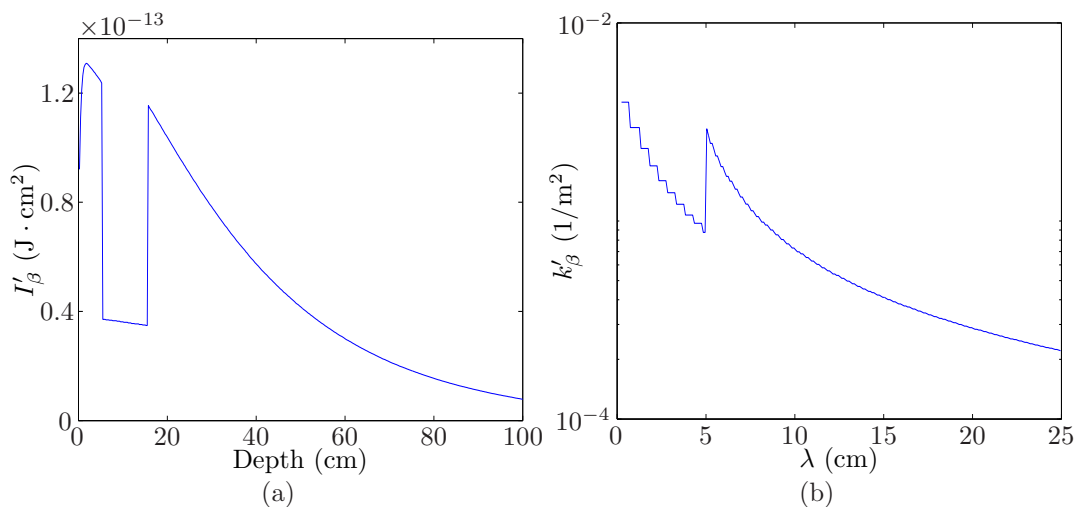

Fig. 10: The effect of a cylindrical insert of density $\rho_w = 0.3$ with a radius of 5 cm and length of 10 cm, located at 5-cm-depth in water, on the individual pencil-beam components. The beamlet going through the center of the cylinder for a 6 MV beam is examined. (a) The heterogeneity corrected depth-directed component $I'_\beta(p_z)$, and (b) the heterogeneity corrected lateral component $k'_\beta(\theta, \lambda, p_z)$ as a function of λ at 10-cm-depth for an angular sector $\theta = [0, \ldots, \pi/8]$.

3.3.4   Build-up and build-down correction

The method described above would result in abrupt changes in the dose level at tissue interfaces, since the scatter originating from the layers above the interfaces is not properly taken into account. To consider the forward-directed energy shift, a build-
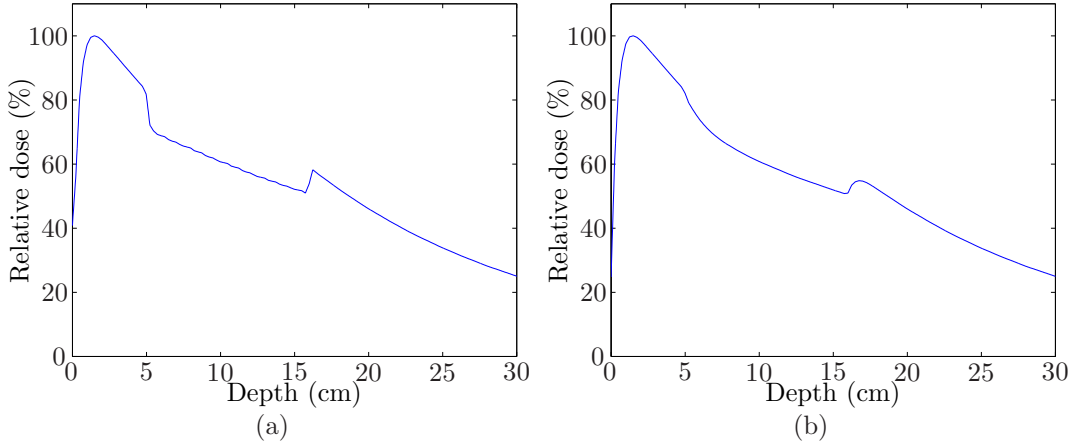
Fig. 11: The calculated dose for a 3×3 cm^2 field for a 6 MV beam incident on a water phantom with lung insert ($\rho_w = 0.3$) from $z = 5, \ldots, 15$ cm (a) without the build-up/build-down correction, and (b) with the correction turned on.

up/build-down correction mechanism was developed. The effect of the correction at the water-lung interface is shown in Fig. 11. To model the gradual changes near interfaces, a convolution with a build-up kernel $k_b(d)$ is performed as a final step of the energy deposition calculation. The kernel is modeled as a superposition of two exponentials:

$$k_{\mathrm{b}}(d) = \begin{cases} \sum_{i=1}^{2} g_i \, \nu_i \, e^{-\nu_i d} & \text{, when } d \geq 0 \\ 0 & \text{otherwise.} \end{cases} \qquad (3.32)$$

Let's define a kernel $\tilde{k}_{\mathrm{b}}(d)$ as k_b in Eq. (3.32), but replacing g_i with $\tilde{g}_i$. Free parameters $\tilde{g}_i$ and ν_i ($i = 1, 2$) are defined such that the squared error between $\tilde{k}_{\mathrm{b}}(d)$ and a function $\tilde{I}_{\mathrm{diff}}(d)$ is minimized. $\tilde{I}_{\mathrm{diff}}(d)$ is computed as:

$$\tilde{I}_{\mathrm{diff}}(d) = \tilde{I}(d + \Delta z) - \tilde{I}(d) * \bar{f}, \qquad (3.33)$$

where $\bar{f}$ is the average attenuation of $\tilde{I}_{\mathrm{diff}}(d)$ in one resolution step. After performing the fit, the weights g_i of k_{b} are then obtained as $g_i = \tilde{g}_i/(\tilde{g}_1 + \tilde{g}_2)$. The I-function at the beam CAX is used to determine $k_{\mathrm{b}}(d)$ i.e. the kernel is assumed to be spatially invariant. An example of the fit between $\tilde{k}_{\mathrm{b}}(d)$ and $\tilde{I}_{\mathrm{diff}}(d)$ for a 6 MV beam is shown in Fig. 12(a). Since the function $\tilde{I}_{\mathrm{diff}}(d)$ characterizes the build-up between vacuum and water, the application of $k_b(d)$ to the energy distribution produces a similar build-up effect in subsequent tissue interfaces. To prevent this energy being shifted to deeper levels, the convolution operation must be pre-compensated in the pencil-beam h_β by performing an inverse convolution (deconvolution) operation at each position (p_x, p_y). Deconvolved function can be calculated by solving $\mathbf{x}$ from the
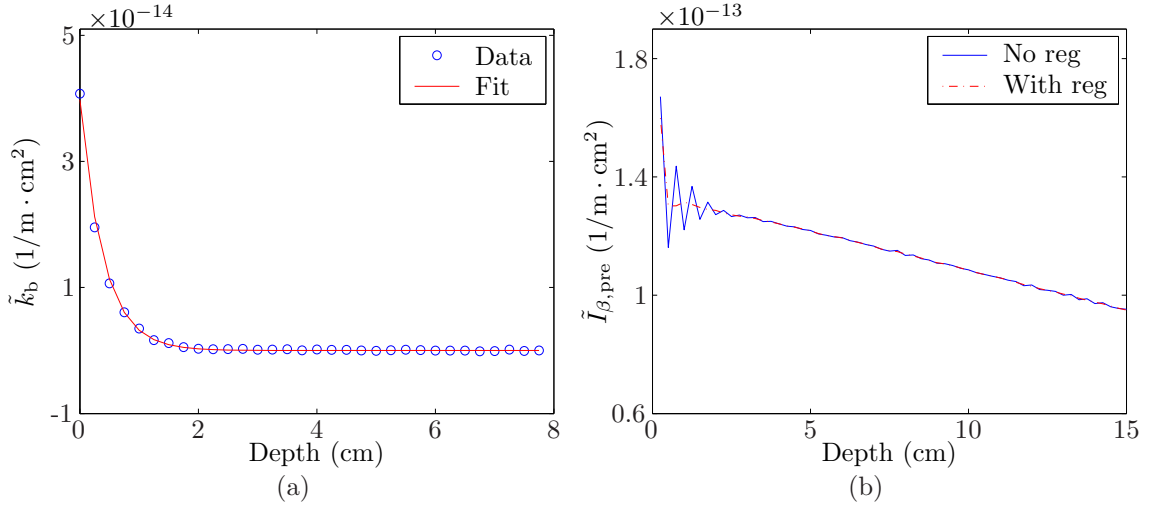
Fig. 12: (a) The non-normalized build-up kernel $\tilde{k}_b(d)$ for a 6 MV beam fitted to the data derived from the depth-directed pencil-beam component. (b) The pre-compensated I-function ($\tilde{I}_{\beta,pre}$) at the CAX for a 6 MV beam without (No reg) and with (With reg) the application of Tikhonov regularization.

following set of linear equations:

$$
\begin{bmatrix}
\Delta z\, k_b(z_0) & \dots & \Delta z\, k_b(z_0 - n\Delta z) \\
\vdots & \ddots & \\
\Delta z\, k_b(z_n) & \dots & \Delta z\, k_b(z_n - n\Delta z)
\end{bmatrix}
\begin{bmatrix}
h_{\beta,\mathrm{pre}}(p_x, p_y, z_0) \\
\vdots \\
h_{\beta,\mathrm{pre}}(p_x, p_y, z_n)
\end{bmatrix}
=
\begin{bmatrix}
h_\beta(p_x, p_y, z_0) \\
\vdots \\
h_\beta(p_x, p_y, z_n)
\end{bmatrix},
$$
$$\underbrace{}_{\mathbf{A}} \quad \underbrace{}_{\mathbf{x}} \quad \underbrace{}_{\mathbf{b}}$$

(3.34)

where $z_0, \dots, z_n$ are the discrete depths, and $h_{\beta,\mathrm{pre}}$ is the pre-compensated pencil-beam for beamlet β. Since the deconvolution is a numerically unstable operation, Tikhonov regularization [63] was applied to penalize for large second derivate of the vector $\mathbf{x}$, which usually corresponds to a noisy function. The regularization can be done by adding the following rows

$$
R = w_{\mathrm{reg}}
\begin{bmatrix}
1 & -2 & 1 & 0 & 0 & \dots & 0 \\
0 & 1 & -2 & 1 & 0 & \dots & 0 \\
\vdots & & & & & & \vdots \\
0 & 0 & \dots & 0 & 1 & -2 & 1
\end{bmatrix},
$$

(3.35)

to the matrix $\mathbf{A}$ of Eq. (3.34), and adding equal number of rows containing zero to the vector $\mathbf{b}$, where w_{reg} controls the strength of the regularization. However, to restrict the number of linear equations, these rows were added to the existing rows in $\mathbf{A}$ instead in order to achieve similar effect. The LU-decomposition was then used to solve Eq. (3.34). In $\mathbf{I}$, the deconvolution was done only for the I-function. However,

that approach was found to result in errors for small field sizes ($\approx 1 \times 1$ cm^2) of high energy beams, and therefore it was later replaced by the deconvolution of the entire pencil-beam along the depth direction.

Instead of the original pencil-beam in Eqs. (3.17)-(3.18), the pre-compensated pencil-beam $h_{\beta,\text{pre}}(p_x, p_y, p_z)$ is used. This results in pre-compensated I- and k-functions: $\tilde{I}_{\beta,\text{pre}}$ and $k_{\beta,\text{pre}}$, respectively. An example of pre-compensated I-function $\tilde{I}_{\beta,\text{pre}}(p_z)$ calculated with and without the regularization is presented in Fig. 12(b), showing the benefit of the regularization. The pre-compensated components replace $\tilde{I}_\beta$ and k_β in the energy deposition of Eqs. (3.26)-(3.27), but otherwise the energy deposition is performed as explained earlier. The convolution with $k_\text{b}(d)$ with the total energy distribution is then performed as

$$E_b(\mathbf{p}) = \int_{v=0}^{p_z} E_\text{total}(p_x, p_y, v) k_b(d_\text{eff}) \rho_\text{w}(p_x, p_y, v) \mathrm{d}v, \qquad (3.36)$$

where d_eff is the signed radiological distance from (p_x, p_y, p_z) to (p_x, p_y, v).

3.3.5 Conversion from energy to dose

In all previous phases, the calculations have been made in terms of energy. As a final step of the calculation, the energy distribution calculated onto the diverging grid is converted into absorbed dose distribution in a Cartesian grid as:

$$D(\mathbf{x}) = \frac{E_b(\mathcal{M}(\mathbf{x}))}{a \, \rho_\text{w}(\mathbf{x}) \, \mathrm{d}V_p}, \qquad (3.37)$$

where $\mathrm{d}V_p$ is the volume element in the diverging grid, and $\rho = a \, \rho_\text{w}$ i.e. mass density ρ is approximated with the relative electron density ρ_w ($a = 1000$ kg/m^3). This approximation is performed, since it was experimentally found to result in good agreement with MC simulations in various heterogeneities. Since the size of the volume element $\mathrm{d}V_p$ is dependent on the distance from target, the conversion in Eq. (3.37) also accounts for SSD variations in different patient geometries.

3.3.6 Computer implementation of the scatter processes

In the computer implementation of the method, Eq. (3.26) is first computed for each beamlet β resulting in a function $I(p_x, p_y, p_z)$. The lateral scattering of energy at the plane p_z for a single exponential component can be efficiently computed using an incremental method, which is equivalent of integrating Eq. (3.27) over an angular sector of width $\pi/8$ and radial length equal to the pixel width. After the weights $\tilde{c}_{ijk}$ have been fitted, the energy d_i to be deposited at pixel i from exponential component

j and angular sector k can be computed as:

$$\begin{cases} d_i &= a_i + s_i - a_{i+1}, \\ s_i &= \tilde{c}_{ijk} I_i, \\ a_{i+1} &= s_i f_i + a_i f_i^2, \\ f_i &= \exp\left(-\frac{1}{2}\mu_j \rho_{\text{w},i} \Delta x\right), \end{cases}$$

where a_i is the amount of energy remaining from earlier pixel contributions along the ray, s_i the fraction of the I-function corresponding to a current angle-range combination, f_i the attenuation of a half width of a pixel, Δx the width of a pixel, and $\rho_{\text{w},i}$ the relative electron density for a pixel i. The "source" contribution (s_i) is attenuated by a half width of a pixel, since it is assumed to originate from the center of the pixel, while the energy contribution from previous pixels (a_i) is attenuated by the full width of a pixel.

The pixel index i is then incremented to span the entire angular sector of the broad beam. The process is repeated for each angular sector and for each of the N exponential components, whereafter the energy depositions are summed up. After the calculation of the scatter for a direction-range pair, a Gaussian smoothing with a small standard deviation is performed to spread the energy deposited by the single ray to the whole angular sector. The process described above corresponds to the computation of Eq. (3.28) for all points $\mathbf{p}$ at depth p_z. The convolution in the depth-direction in Eq. (3.36) is performed with the same algorithm as the scattering along the plane, but now the weights of exponentials in the kernel (g_i) are constant over depth, and there remain only two ranges to be calculated.

4 Beam characterization techniques

In this chapter, the beam model of **II** developed for the kernel-based dose calculation method is described together with the procedure for adapting the model for an individual treatment unit. The differences in the modeling of standard and FFF beams desribed in **V** are also presented. Finally, the principles for incorporating the developed beam model into a MC based transport algorithm developed in **IV** are described.

4.1 Multiple-source model for clinical photon beams

The radiation beam produced by a medical linac consists mainly of the bremsstrahlung (primary) photons that result from radiative interactios between the impinging electrons and the atomic nuclei in the target material. Most linac models include a flattening filter to generate a uniform dose distribution at some depth in a flat phantom [10]. As the primary radiation traverses through the flattening filter, the spectrum becomes harder (mean energy increases), since the low energy photons are more likely to interact in the filter. The primary photon spectrum becomes spatially varying, since thinner portions of the filter produce less spectral hardening. Also the energy fluence after the flattening filter varies slightly within the beam area.

In addition to the primary (focal) radiation, the beam also contains significant amount of photons that have interacted in some other treatment head component. The magnitude of this extra-focal radiation is on the order of 10% of the total energy fluence exiting the treatment head, depending on the field size and the treatment head structure. Mainly, it originates from the primary collimator and from the flattening filter, and has a small contribution ($\approx 1\%$ of total dose) from the movable jaws [10]. Due to larger divergence, the effect of the extra-focal radiation is most prominent in the region outside the geometric field edge. The clinical photon beam also contains charged-particle contamination, which results from interactions occurring mainly in flattening filter, movable jaws, and in the air column between the patient and the target. The contamination electrons (and positrons) contribute significantly to the total dose distribution only in the build-up region. If additional accessories, such as wedges or compensators, are present in the field, they act as sources for scattered photons and charged particles, but also remove these particles from the beam.

For a given point in the target volume, the changes in the output factor (Gy/MU) as a function of field size result mainly from the changes in phantom and head scatter components. However, some of the photons directed towards the jaws are scattered back to the monitor chamber. This backscatter component is largest when the jaw

opening is small, in which case the irradiated area of the jaws is largest. For the accurate calculation of MUs i.e. absolute dose, the backscatter has to be modeled as well.

For all major radiation components in the beam, the kernel-based dose calculation method developed in **I** requires as an input a spatially varying energy fluence spectrum $\Psi_E(E; x, y)$. To generate this information, an MSM was developed. It consists of separate sub-sources: one for primary photons, another for extra-focal photons, and a third one for contamination electrons. In addition, for hard wedges, the model includes an extra source for the photons that interact with the wedge material. The presented model is similar to those virtual source models described in the literature [39, 42], although the modeling of the spatially varying primary photon spectrum is potentially more accurate than the prior methods due to increased flexibility. There exist also some enhancements in the modeling of extra-focal photons as compared to the other models. However, the parameterization of the beam model and the automatic procedure for deriving the free parameters from basic measurements can be considered as the largest improvements over prior work.

4.1.1 Primary photon source

In the developed MSM, the primary photons are assumed to originate from a point-like source located at the target. Alternatively, a finite-size source could have been used [42], and the source position could have been derived from the MC simulated distribution of interaction positions [39]. The initial spectrum $\Psi_{E,\mathrm{init}}$ of the bremsstrahlung photons was derived from MC simulations with the BEAMnrc code [33] for nominal energies from 4 MeV to 25 MeV. The target materials and thicknesses were obtained from the specifications of Varian treatment units, but it is worth to know that the same spectra are also applied for the units built by other manufacturers [**II**]. In the simulations, the energy of the electron beam was assumed to be equal to the beam nominal energy, and its intensity distribution was modeled with a 2D Gaussian using a full width at half maximum value of 1.0 mm. When an exponential attenuation is performed for each energy component, the spectrum below the flattening filter can be expressed as [**II**]:

$$\Psi_{E,\mathrm{ff}}(E; r) = \Psi_{E,\mathrm{init}}(E) \exp\left[-\mu/\rho(E) d_{\mathrm{ff}}(r)\right], \qquad (4.1)$$

where $\mu/\rho(E)$ is the mass attenuation coefficient for energy E of the given the flattening filter material, and $d_{\mathrm{ff}}(r)$ is the mass thickness of the flattening filter at position r, which is unknown at this point. Instead of using specifications provided by the manufacturer in order to obtain $d_{\mathrm{ff}}(r)$, the spectrum below the flattening filter was parameterized with a curve $\bar{E}(r)$. The discrete points determining $\bar{E}(r)$, which describes the mean energy below the flattenning filter, are free parameters in the

model. The mass thickness $d_{\text{ff}}(r)$ can be determined in an iterative way when $\bar{E}(r)$ is known by requiring that $<\Psi_{E,\text{ff}}>(r) = \bar{E}(r)$. Another choice for modeling the off-axis softening would have been an analytical function with a few free parameters to model the CAX spectrum, which would be scaled with a pre-determined correction factor dependent on r to obtain the spectrum at other positions [42]. However, the presented model has the benefit of adjusting the off-axis softening for each individual treatment unit, while keeping the number of free parameters small (≈ 6).

The mean radial energy curve $\bar{E}(r)$ is also used for modeling FFF beams in $\mathbf{V}$, since the initial bremsstrahlung spectrum varies slightly as a function of off-axis position in the beam. The use of $\bar{E}(r)$ also compensates for any inaccuracies in the electron beam energy in the BEAMnrc simulations, which were used to derive the initial spectra $\Psi_{E,\text{init}}$.

In case of hard wedge, the spectrum of primary photons is no longer radially symmetric. The 2D spectrum below the wedge can be calculated by further attenuation of the spectrum $\Psi_{E,\text{ff}}(E;r)$ at each (x,y) position using the estimated wedge mass thickness $d_{\text{wedge}}(x,y)$ along the ray from the source to the point (x,y) at the isocenter plane. In this case, $d_{\text{wedge}}(x,y)$ is determined iteratively using the information about transmission $t(x,y)$, which describes the fraction of energy remaining in the beam after it traverses the wedge. This information is obtained by requiring that $t(x,y) = \Psi_{\text{wedge}}(x,y)/\Psi_{\text{ff}}(x,y)$, where $\Psi_{\text{wedge}}(x,y)$ is the energy fluence below the wedge. The wedge transmission $t(x,y)$ is obtained via optimization from the wedge profile and the wedge PDD measurements (see Sec. 4.2). Other accessories, such as the MLC, block, enchanced dynamic wedge (EDW) or compensator are assumed to have no effect on the spectrum, although this is only a rough estimate for physical compensators.

The shape of the energy fluence distribution for primary photons below the flattening filter is modeled using an intensity profile curve $I(r)$, where the discrete points defining the curve are free parameters. It is relatively flat for standard beams, but is bell-shaped for FFF beams due to missing attenuation in the flattening filter. The energy fluence for the primary photons $\Psi_{\text{prim}}(x,y)$ at the isocenter plane in air is then computed as [$\mathbf{II}$]:

$$\Psi_{\text{prim}}(x,y) = I(r) \prod_{i=1}^{N} F_i(x,y), \tag{4.2}$$

where $r = (x^2 + y^2)^{-1/2}$ and F_i is a modulating function for a device i. However, the energy fluence is normalized such that $\Psi_{\text{prim}}(0,0) = 1$. Hence, the beam model only gives the shape of the energy fluence distribution, not the absolute level. For jaws, static MLCs and blocks, the modulating function is unity inside the field opening, and user given material transmission outside the opening. For compensators and
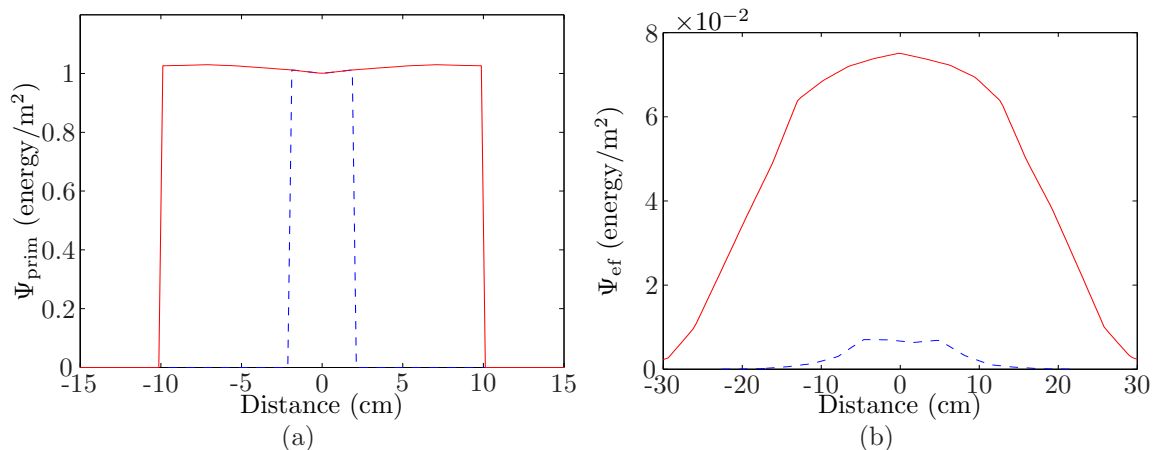
Fig. 13: The normalized energy fluence for the primary (a) and the extra-focal (b) photon sources for open fields of sizes 4×4 (dotted line) and 20×20 cm^2 (solid line). The fluence profile along direction of the lower jaw (X) at $y = 0$ and $z = d_{SAD}$ is shown.

hard wedges, the modulation equals the transmission map $t(x, y)$ described above. In IMRT fields, the modulating function is obtained from a separate leaf motion calculator, which accounts for the leaf transmission, rounded leaf tips and tongue-and-groove (TG) effects. The individual leaves of some MLC models have a so-called TG or a stepped-edge design to minimize the inter-leaf leakage, which has the drawback of creating areas of underdosage in IMRT fields that needs to be modeled. The energy fluence for an EDW is computed as a weighted sum of the energy fluences of the individual jaw openings of the field, weighted by the number of MUs spent at each position.

Compared with the beam model presented in **II**, the current model considers also the finite spot size of the bremsstrahlung target. It is modeled by smoothing the primary fluence of Eq. (4.2) with a 2D Gaussian, which has user-defined width parameters in x- and y-directions. This modeling was found to improve the match between measured and calculated field penumbra, particularly for Siemens Primus and Elekta Beam Modulator linac models.

4.1.2 Extra-focal photon source

The extra-focal photon radiation is modeled using an extended source located at the bottom plane of the flattening filter (distance z_{ff} from target). The use of one effective source instead of several sources (cf. [41]) is justified, since most of the extra-focal radiation originates from the flattening filter and from the primary collimator, which are located close to each other in the treatment head. The intensity distribution of the extended source is modeled with a Gaussian, which is supported by the experimental findings [64] and the MC simulations [39]; although also uniform [65] and triangular [43] distributions, as well as a sum of Gaussians [40] have

been used. The energy fluence at an arbitrary depth z can then computed by ray-tracing from the source to the destination plane through the beam limiting devices as:

$$\Psi_{\text{ef}}(x, y, z) = w_{\text{ef}} \iint \frac{\cos \theta}{r^2} G(x', y') \, t \, \mathrm{d}x' \, \mathrm{d}y', \qquad (4.3)$$

where w_{ef} is the weight factor, θ the angle between the ray from (x', y', z_{ff}) to (x, y, z) and the z-axis, r the distance between the source and destination pixels, and $G(x', y')$ the value of the Gaussian at (x', y'). The value of multiplier t is zero, if the corresponding ray intersects with jaws, MLC or block, and otherwise it is unity. The cosine term in Eq. (4.3) results from the planar geometry, where the area element at the destination plane is not perpendicular to the ray originating from the source plane. The width of the Gaussian at the source plane σ_{ef} and the weight w_{ef} are free parameters in the model. An example of the primary and extra-focal energy fluences is presented in Fig. 13. The fluence computation in Eq. (4.3) explicitly accounts for the distances of the upper and lower jaws and MLC from the target, which was not the case with the earlier models (cf. [39]). This was found to be important for accurate absolute dose calculations of small MLC apertures within a larger jaw opening (see Fig. 9 in **III**).

The spectrum of the extra-focal photons $\Psi_{E,\text{ef}}(E)$ is assumed to be constant across the broad beam, which is a reasonably good approximation based on the results from MC simulations [66]. The spectrum is modeled using an empirically derived template spectrum, and a mean energy $\bar{E}_{\text{ef}}$ (a free parameter). The energy axis of the template spectrum is scaled in an iterative process such that the mean energy matches with the optimized value. This is a rough approximation of the shape of the spectrum, but it has been proven to be sufficient for clinical dose calculations.

The extra-focal source described above was used also for the modeling of FFF beams in **V**. However, further tests with asymmetric fields revealed that better agreement to experimental data can be obtained by turning the extra-focal source off. This is due to significantly smaller head scatter component in FFF beams compared to standard beams, since the flattening filter is not present in the beamline. A smaller contribution of head scatter from the primary collimator remains, but this cannot be apparently well modeled with a Gaussian plane source. However, the observed deviations for FFF beams were smaller than 3% even though no extra-focal source was in use.

4.1.3 Electron contamination source

The model for the contamination electrons for standard and FFF beams is empirical, and it is based on the assumption that the difference between the measured and the calculated photon PDD is due to contamination electrons. The energy fluence of the contamination electrons is modeled as a convolution of the primary energy fluence

with a dual Gaussian kernel. Two Gaussian components were required to model the field size dependence with sufficient accuracy down to small field sizes. Therefore, the calculation of the electron contamination fluence $\Psi_{\mathrm{el}}(x,y)$ can be written as:

$$\Psi_{\mathrm{el}}(x,y) = \sum_{i=1}^{2} c_i \Psi_{\mathrm{prim}}(x,y) \otimes G_i(x,y), \tag{4.4}$$

where c_i is the weight of component i, $G_i(x,y)$ the Gaussian kernel with width $\sigma_{e,i}$, and $\otimes$ the convolution operator. Parameters c_1, $\sigma_{e,1}$ and $\sigma_{e,2}$ are free parameters in the model ($c_2 = 1 - c_1$). Eq. (4.4) implicitly models the field-size dependence, since the decrease in the width of the primary fluence leads to a smaller convolution result at the CAX. The total energy deposited per unit length $c_{\mathrm{e}}(z)$ in a water-equivalent material is modeled as:

$$c_{\mathrm{e}}(z) = \sum_{i=1}^{N} w_{\mathrm{e},i} \exp(-k_i z), \tag{4.5}$$

where the attenuation coefficients k_i are fixed, and the weights $w_{\mathrm{e},i}$ are optimized based on the measured PDD for the largest field size, as will be described in Sec. 4.2. The value $N = 6$ was used in Eq. (4.5), since this was found to result in a good fit to that part of the measured PDD, which was assumed to originate from electron contamination. The combination of a Gaussian lateral dependency with an exponential depth dependency has also been successfully used by other authors [21]. However, the presented model is somewhat more flexible than most prior models, since e.g. the build-up in the electron PDD seen in high-energy beams can be modeled with Eq. (4.5). Since a large fraction of the contamination electrons is created in air, the size of the air column between the target and the patient has a considerable effect on the electron contamination. However, this effect cannot be taken into account with the current model, but would require a more physics-based description of the phenomenon.

4.1.4 Wedge scatter source

The developed MSM includes a sub-source for the photons that interact in the hard wedge. The wedge filter is the next largest source of scatter in wedged beams after the flattening filter and primary collimators [10]. The energy fluence of the wedge scatter is modeled similarly to the contamination electrons in Eq. (4.4), but the parameters for the Gaussians have been pre-calculated based on MC simulations. The width parameters of the Gaussians and their relative weights are dependent on the wedge angle and the nominal energy of the beam. The primary fluence, which is used in the convolution process, is taken above the wedge. A total weight factor w_{ws}, which multiplies the convolution result, is used as a free parameter in the model.

The spectrum of the photons scattering from the wedge is modeled analogously to the extra-focal photons.

4.2 Adapting the beam model to individual treatment units

Medical linacs have individual differences, not only between the treatment units of different vendors, but also between the units of same model and vendor. Sometimes the treatment units are also calibrated differently depending of the wishes of the users. The developed MSM contains free parameters that can be adjusted for each individual treatment unit. An automatic optimization process for the derivation of the free parameters from basic water-phantom measurements was presented in **II**, and its main features are described in this section. In a clinical use, the medical physicist runs the algorithm, and automatically obtains optimized parameter values for the particular beam. In some other model-based photon dose calculations systems, the physicist is required to perform time-consuming manual parameter fitting [67] or to send the measured data to the vendor of the TPS for centralized processing [43].

4.2.1 The optimization process for deriving model parameters

The set of measurements used for deriving the model parameters consists of PDDs for several square fields, profiles at several depths for the same fields, and diagonal profiles for the largest rectangular field. In addition, the measured output factors for several rectangular fields are required to model the backscatter. For MU calculation, the treatment unit calibration (Gy/MU) at a certain reference geometry is also needed. The free model parameters for an open beam are then derived using the following process:

1. Checking of the input measurement data for common errors, and making necessary modifications to the measured data.

2. Initial optimization of the parameters for the primary and extra-focal photon source $[\bar{E}(r), I(r), w_{\text{ef}}, \sigma_{\text{ef}}, \bar{E}_{\text{ef}}]$ by minimizing an objective function quantifying the deviation between measurements and calculations performed with a fast point dose calculation method $M_{\text{p.d.}}$ (see Sec. 4.2.3). The measurements in the build-up region are ignored in this phase.

3. Optimization of the electron contamination parameters $[c_1, \sigma_{\text{e},1}, \sigma_{\text{e},2}, w_{\text{e},i} \ (i = 1, \ldots, 6)]$ based on the remaining difference between the measured and the calculated PDDs. The volumetric dose calculation method of Sec. 3.3, denoted here as $M_{\text{v.d.}}$, is used in this phase.

4. Evaluation of the differences between the two dose calculation methods ($M_{\text{v.d.}}$ and $M_{\text{p.d.}}$) at the current parameter values. The measured beam data, which

are used as an optimization target, are replaced by the original measurements subtracted by the differences.

5. Refining the primary and extra-focal photon source parameters using the full set of measured data (including the build-up region) in the optimization.

6. Calculation of parameters, which describe the backscatter and the calibration factor required for MU calculation.

In the method proposed above, both profile and PDD measurements for several field sizes are used simultaneously to determine the beam model parameters, since the effects of different parameters are not independent of each other. This approach is different from the technique used by the other authors [42,43], where the spectrum parameters are derived from PDD data, and the energy fluence parameters from the profile data. Several authors [40,42] have used the nonlinear χ^2-minimization using the Levenberg-Marquardt algorithm [61], although it requires the computation of the gradient of an objective function that limits its functional form.

4.2.2 The objective function

The objective function $f(\mathbf{x})$ to be minimized in steps (2) and (5) is of the form:

$$f(\mathbf{x}) = f_{\text{penalty}}(\mathbf{x}) \times \sum_{i=1}^{K} w_i \hat{\gamma} \left(\mathbf{D}^{\text{c}}(\mathbf{x}), D_i^{\text{m}} \right), \tag{4.6}$$

where K is the total number of measurement points in the PDDs and profiles, $\mathbf{x}$ the vector containing the current parameter values, $f_{\text{penalty}}(\mathbf{x})$ the penalty term, w_i the weight factor for point i, and $\hat{\gamma}$ the gamma error between the measurement D_i^{m} and the corresponding calculated curve $\mathbf{D}^{\text{c}}(\mathbf{x})$. The gamma index introduced by Low et al. [68] combines the dose-difference and the distance-to-agreement (DTA) error criteria, and therefore it can be used in both low and high-gradient areas of the dose distribution. When considering a dose measurement $D_m(\mathbf{r}_m)$ at position $\mathbf{r}_m$ and a calculated dose curve $\{\mathbf{r}_c, D_c(\mathbf{r}_c)\}$, the gamma index γ is defined as [68]:

$$\gamma(\mathbf{r}_m) = \min_{\mathbf{r}_c} \left\{ \Gamma(\mathbf{r}_m, \mathbf{r}_c) \right\}, \tag{4.7}$$

where

$$\Gamma(\mathbf{r}_m, \mathbf{r}_c) = \sqrt{\frac{r^2(\mathbf{r}_m, \mathbf{r}_c)}{\Delta d_M^2} + \frac{\delta^2(\mathbf{r}_m, \mathbf{r}_c)}{\Delta D_M^2}}, \tag{4.8}$$

$r(\mathbf{r}_m, \mathbf{r}_c) = |\mathbf{r}_m - \mathbf{r}_c|$, $\delta(\mathbf{r}_m, \mathbf{r}_c) = D_c(\mathbf{r}_c) - D_m(\mathbf{r_m})$, Δd_M is the DTA criterion and ΔD_M the dose-difference criterion. In this work, the values $\Delta d_M = 3$ mm and $\Delta D_M = 1\%$ were used. Eq. (4.7) defines the shortest distance between the measurement point and the calculated curve in a combined dose-distance scale (see

Fig. 14). See Fig. 15 for the application of the gamma index in the quantification of deviation between measured and calculated dose profiles. In the proposed method,
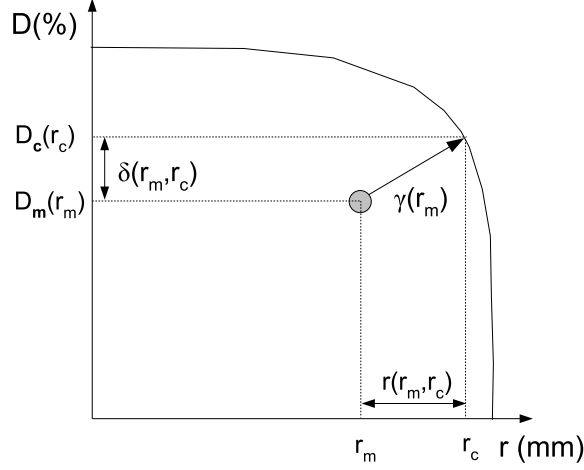

Fig. 14: An illustration of the gamma index between the measurement point $D_m(\mathbf{r}_m)$ and the calculated curve $\{\mathbf{r_c}, D_c(\mathbf{r}_c\})$.
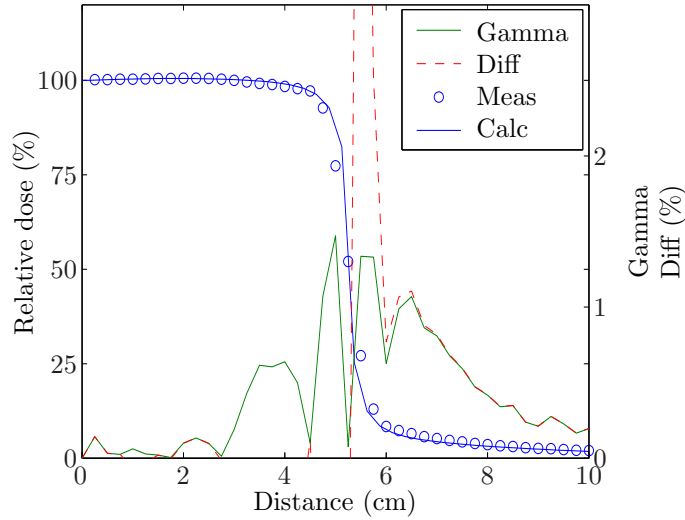

Fig. 15: Comparison of gamma index (Gamma) and dose difference (Diff) in the quantification of the deviation between measured (Meas) and calculated (Calc) dose profiles.

the gamma index of Eq. (4.7) is further modified such that $\hat{\gamma}(\cdot) = 3\gamma(\cdot)^2 + \gamma(\cdot)$, where $(\cdot)$ stands for the arguments presented in Eq. (4.6). The quadratic term is used to penalize more for large deviations, and the linear term is used to have a larger gradient near the optimum location to better guide the optimization process. The penalty term $f_{\text{penalty}}(\mathbf{x})$ is applied in order to avoid the characterization of noisy measurements and to restrict the parameters into a reasonable physical range.

64

4.2.3 Fast point dose calculation method

In the proposed process, the dose is calculated thousands of times during the process for the set of K points. The use of the volumetric method $M_{v.d.}$ of Sec. 3.3 would be too slow for this purpose, and hence a faster point dose calculation method was developed. The faster method $M_{p.d.}$ is capable of reproducing $M_{v.d.}$ calculations for open fields in water, except for the electron contamination component. Hence, the faster method is much more limited and does not work e.g. in heterogeneous phantoms. The same monoenergetic pencil-beams are used as in $M_{v.d.}$, but the division into depth-directed and lateral components is not performed. Instead, the dose at the calculation point is obtained as a superposition of the contributions of monoenergetic kernels in each grid point surrounding the calculation point. Each contribution is a direct look-up from the pencil-beam, weighted by the corresponding spectrum component defined at the grid point, the intensity profile value and the grid area.

The calculation for a discrete set of points can be written as:

$$\mathbf{d}_{p.d.} = \mathbf{A}_{prim}\mathbf{s}_{prim} + w_{ef}\mathbf{A}_{ef}\mathbf{s}_{ef}, \tag{4.9}$$

where $\mathbf{d}_{p.d.}$ is the calculated dose for the set of K points, $\mathbf{A}_{prim}$ the primary dose deposition matrix, $\mathbf{s}_{prim}$ the vector containing the product of the radial energy spectrum and intensity profile values at discrete radii and energy bins, w_{ef} the weight of the extra-focal source, $\mathbf{A}_{ef}$ the extra-focal dose deposition matrix, and $\mathbf{s}_{ef}$ the vector containing the extra-focal photon spectrum at discrete energy bins. Using the formalism of Eq. (4.9), the repetitive computations become very efficient, since in most cases only $\mathbf{s}_{prim}$ or $\mathbf{s}_{ef}$ need to be re-evaluated when the parameter values are modified.

The method $M_{p.d.}$ agrees well with the results of $M_{v.d.}$ except in the build-up region. However, the agreement does not have to be exact, since the difference between $M_{p.d.}$ and $M_{v.d.}$ is taken into account in the optimization process. In step (4) of the optimization process, the measurement data $\mathbf{D}^m$, which is used as the optimization target, is replaced with a modified set of measurements $\mathbf{D}^m_{mod}$ defined as:

$$\mathbf{D}^m_{mod} = \mathbf{D}^m - \mathbf{D}_{diff}(\mathbf{x}^*) = \mathbf{D}^m - [\mathbf{D}_{v.d.}(\mathbf{x}^*) - \mathbf{D}_{p.d.}(\mathbf{x}^*)], \tag{4.10}$$

where $\mathbf{x}^*$ is the optimal set of parameters reached after the step (3), and $\mathbf{D}_{v.d.}(\mathbf{x}^*)$ and $\mathbf{D}_{p.d.}(\mathbf{x}^*)$ are the set of doses calculated using $M_{v.d.}$ and $M_{p.d.}$, respectively. During the optimization process, the parameter values are modified such that $\mathbf{D}_{p.d.}(\mathbf{x})$ converges to $\mathbf{D}^m_{mod}$. As a consequence, $\mathbf{D}_{v.d.}(\mathbf{x})$ converges to the original measurements $\mathbf{D}^m$ provided that $\mathbf{D}_{diff}(\mathbf{x})$ remains constant.

4.2.4 Powell's direction search and line minimization methods

To determine the optimal set parameters $\mathbf{x}^*$ in the steps (2) and (5), the objective function $f(\mathbf{x})$ of Eq. (4.6) needs to be minimized. Since the analytical calculation of the gradient is difficult, the Powell's direction search method [69], which does not require a gradient calculation, was selected. For this specific problem, it was found to be faster than another feasible choice, i.e. the downhill Simplex method [70]. The Powell's method is based on line minimizations along a set of search directions and on the calculation of a new direction based on the position reached in the search space. The method is guaranteed to be able to find the exact minimum of a quadratic function in a finite number of iterations, but it is not guaranteed to find the global minimum. However, since the objective function of Eq. (4.6) is nearly quadratic and heuristic penalty terms are used to restrict the parameter values, it is unlikely that multiple local minima will occur in practise.

Initially, n linearly independent search directions $\mathbf{d}_1, \ldots, \mathbf{d}_n$ are selected (n is the dimension of the search space). These directions can be chosen e.g. to be equal to the coordinate directions. An initial guess $\mathbf{x}_0$ for the parameter vector is required. Then for each i ($i = 1, \ldots, n$), a scalar λ_i is determined such that [69]

$$\lambda_i = \arg \min_\lambda f(\mathbf{x}_{i-1} + \lambda \mathbf{d}_i). \tag{4.11}$$

The parameter vector is updated accordingly as [69]:

$$\mathbf{x}_i = \mathbf{x}_{i-1} + \lambda_i \mathbf{d}_i. \tag{4.12}$$

After the above process has been repeated for each of the n directions, a new conjugate direction $\mathbf{d}_{\mathrm{conj}}$ is calculated as [69]:

$$\mathbf{d}_{\mathrm{conj}} = (\mathbf{x}_n - \mathbf{x}_0)/\|\mathbf{x}_n - \mathbf{x}_0\|, \tag{4.13}$$

where $\mathbf{x}_n$ is the parameter vector after the nth line minimization. Then, one additional line minimization is performed along $\mathbf{d}_{\mathrm{conj}}$. One of the existing search directions $\mathbf{d}_i$ is also replaced by $\mathbf{d}_{\mathrm{conj}}$, if the determinant of resulting set of search directions does not decrease. These $n+1$ line minimizations constitute one iteration of the Powell's method, and the process is iterated until a specified stopping criterion is reached. For example, the procedure can be stopped when the improvement in the objective function value during one iteration is smaller than a certain threshold value. See Fig. 16(a) for an example of the Powell's method applied to a function of two variables.

In this work, a golden section search and a parabolic interpolation are used to solve the 1D minimization problem of Eq. (4.11). The golden section search [61] is
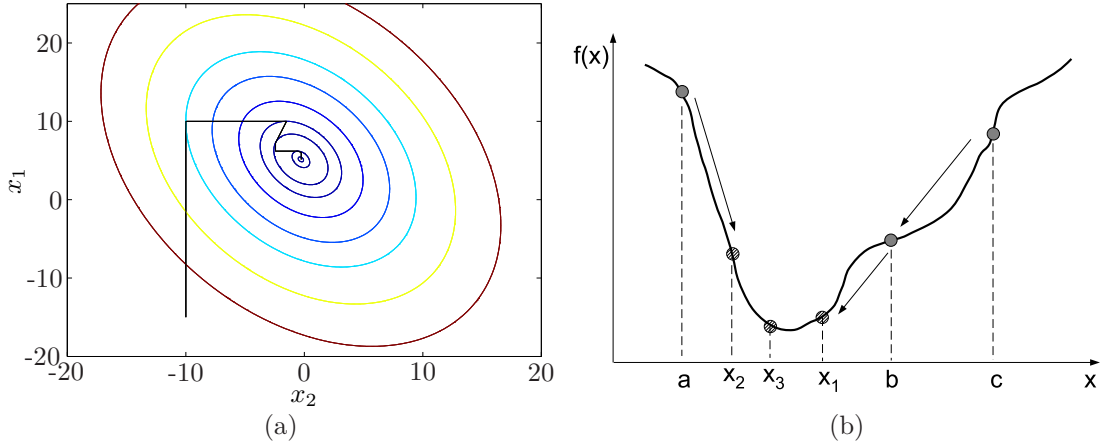
Fig. 16: (a) Powell's direction search method applied for the minimization of a function $f(x_1, x_2) = (x_1 - 5)^2 + 2(x_2 - 1)^2 + x_1 x_2$. (b) An illustration of a golden section search in 1D minimization problem. The search starts from a triplet (a, b, c), which brackets the minimum. After the function evaluation at x_1, the minimum is bracketed by the points (a, x_1, b); then again at x_2 resulting in (x_2, x_1, b); and finally at x_3, resulting in a bracketing triplet (x_2, x_3, x_1), (modified from [61]).

the optimal strategy for reducing the search interval, if there is no *a priori* information about the function. Let's denote the function along the ith search direction $f(\mathbf{x}_{i-1} + \lambda \mathbf{d}_i)$ by $f(\lambda)$. The golden section search starts from a triplet of points (a, b, c) such that $f(b) < f(a)$ and $f(b) < f(c)$, so that $f(\lambda)$ has exactly one minimum within the interval $[a, c]$. Then the algorithm proceeds by selecting a point x, which divides the larger interval into two sections according to the golden ratio. The function is then evaluated at the new point: if $f(x) < f(b)$, the new triplet bracketing the minimum is (a, x, b); otherwise the triplet is (x, b, c). This process is then repeated until the length of the search interval is smaller than a given tolerance. In Fig. 16(b), the process of shrinking the search interval is illustrated. The golden section search is applied during the first iteration of the Powell's search, when the changes in the parameter values are large. In subsequent iterations, the faster parabolic interpolation [61] is used, since the function can be assumed to be parabolic close to the minimum. In the parabolic interpolation, a parabola is fitted to the three known points $\{a, f(a)\}$, $\{b, f(b)\}$ and $\{c, f(c)\}$, and the minimum position of the parabola is used as an approximate solution of the 1D minimization problem.

4.2.5 Optimization of electron contamination parameters

In this work, it is assumed that the difference between measured PDDs and calculated PDDs (without electron contamination) is caused by a charged-particle contamination. An additional assumption is that the shape of electron contamination PDD is the same for all field sizes i.e. that only the relative magnitude

varies. To derive the optimal values for c_1, $\sigma_{e,1}$ and $\sigma_{e,2}$, the difference curves $\delta_i(z) = \text{PDD}_{\text{meas},i}(z) - \text{PDD}_{\text{v.d.},i}(z)$ are evaluated for each field size FS_i $(i = 1, \ldots, N)$ up to the depth of corresponding maximum range of the contamination electrons. Then, the optimal scaling factors $w_{i,\text{target}}$, which describe how much the difference curve of the largest field size $\delta_N(z)$ needs to be scaled to obtain $\delta_i(z)$, are determined. The weights that give the least squares solution by minimizing $\|\delta_i - w_{i,\text{target}}\delta_N\|$ are obtained as

$$w_{i,\text{target}} = \delta_N^{\text{T}} \delta_i \, (\delta_N^{\text{T}} \delta_N)^{-1}, \tag{4.14}$$

where the vector δ_i contains the dose differences for the field size FS_i at discrete depths. The calculated scaling factors $w_{i,\text{calc}}$ are obtained by performing a convolution of a square fluence of side length FS_i with both of the Gaussian kernels and superimposing the results with weights c_1 and $1 - c_1$. The scaling factor $w_{i,\text{calc}}$ equals the value of the convolution at the beam CAX normalized by the convolution result for the largest field size. The result of the convolution at CAX can be computed efficiently using the error function $\text{erf}(x)$:

$$w_{i,\text{calc}} = c_1 \, \text{erf}\left[\text{FS}_i/(2\sqrt{2}\,\sigma_{e,1})\right] + (1 - c_1)\,\text{erf}\left[\text{FS}_i/(2\sqrt{2}\,\sigma_{e,2})\right]. \tag{4.15}$$

The parameters c_1, $\sigma_{e,1}$ and $\sigma_{e,2}$ are then obtained by minimizing the objective function $f_{\text{obj,e}}$, which is defined as:

$$f_{\text{obj,e}}(c_1, \sigma_{e,1}, \sigma_{e,2}) = \sum_{i=1}^{N}(w_{i,\text{target}} - w_{i,\text{calc}})^2 + f_{\text{sim}}(\sigma_{e,1}, \sigma_{e,2}), \tag{4.16}$$

where $f_{\text{sim}}(\cdot)$ penalizes for parameters $\sigma_{e,i}$ $(i = 1, 2)$ that have too similar values. The minimization is performed using the Powell's method described in Sec. 4.2.4. An example of the optimal and fitted scaling factors is shown in Fig. 17(a), and the difference curves derived from the measurements and the fitted curves $\delta_{i,\text{fit}}(z) = w_{i,\text{calc}}\delta_N(z)$ are shown in Fig. 17(b).
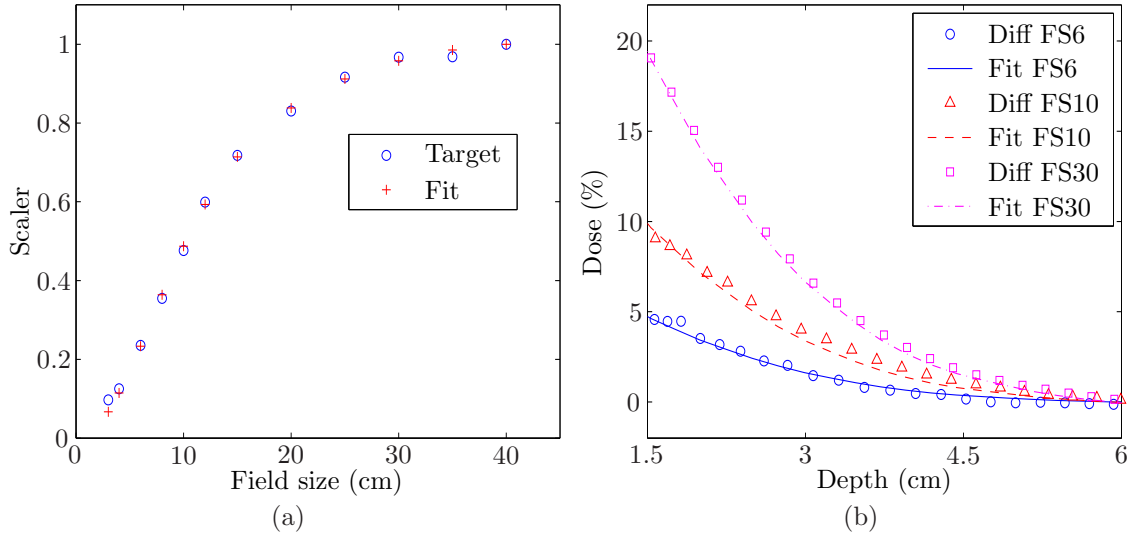
Fig. 17: (a) A comparison of the optimal and fitted scaling factors ($w_{i,target}$ vs. $w_{i,calc}$), which model the field size dependence of the electron contamination for a Varian 6 MV beam. (b) The actual difference curves $\delta_i(z)$ compared to the fitted curves obtained as $\delta_{i,fit}(z) = w_{i,calc}\delta_N(z)$ for field sizes (FS) 6, 10 and 30 cm.

After the shape parameters of the Gaussians have been derived, the curve $c_e(z)$ of Eq. (4.5) can be determined. For each exponential component $c_{e,i}(z) = \exp(-k_i z)$ ($i = 1, \ldots, 6$), the corresponding PDD $d_{e,i}(z)$ is calculated with $M_{v.d.}$. There is linear relationship between the component $c_{e,i}(z)$ and the corresponding depth dose $d_{e,i}(z)$. Hence, the weights $w_{e,i}$ of Eq. (4.5) can be determined by solving the following matrix equation in the least-squares sense:

$$\underbrace{\begin{bmatrix} d_{e,1}(z_1) & \ldots & d_{e,6}(z_1) \\ \vdots & \ddots & \\ d_{e,1}(z_M) & \ldots & d_{e,6}(z_M) \end{bmatrix}}_{\mathbf{D}} \underbrace{\begin{bmatrix} w_{e,1} \\ \vdots \\ w_{e,6} \end{bmatrix}}_{\mathbf{w}} = \underbrace{\begin{bmatrix} \delta_N(z_1) \\ \vdots \\ \delta_N(z_M) \end{bmatrix}}_{\delta_{\mathbf{N}}}, \qquad (4.17)$$

where $z_1, \ldots, z_M$ are the discrete points in the depth direction.

4.2.6 Modeling of hard wedges

The parameters for the hard wedge model are derived after the open field has been optimized. The free parameters are the transmission curve $t(y)$, the weight w_{ws}, the mean energy $\bar{E}_{ws}$ for the wedge scatter source, and the electron contamination parameters that replace those of the open field. For Varian wedges, the transmission is only a function of the distance y along the wedge direction, since the thickness of the physical wedge is constant along the perpendicular direction. The wedge

parameters in the current model are derived in an analogous way to the open field using the Powell's method for the minimization. The parameter vector $\mathbf{x}$ consists of the discrete points determining the transmission curve $t(y)$, and of the wedge scatter parameters w_{ws} and $\bar{E}_{\mathrm{ws}}$. Electron contamination parameters are defined similarly to open fields. Wedge PDD and profile measurements for several field sizes, as well as the longitudinal profile for the largest field size, are used as an optimization target. The wedge model has been improved from the one used in **III**, where the parameters were derived based only on a single wedge profile and a single longitudinal profile, and the electron contamination parameters for open field were used. These approximations caused large discrepancies, particularly in the build-up region of high energy beams.

4.2.7   Monitor unit calculation

It is necessary that a photon dose calculation algorithm designed for clinical use is also capable of calculating the MUs required to achieve the prescribed dose (Gy) at a reference point in the patient. The MUs for an arbitrary field with the jaw settings $X \times Y$ can be calculated based on the known treatment unit calibration as:

$$\mathrm{MU} = \mathrm{CBSF}(X, Y)(\mathrm{MU/Gy})_{\mathrm{calib}}(D_{\mathrm{calib}}/D_{\mathrm{pre}})\mathrm{Gy}_{\mathrm{pre}}, \tag{4.18}$$

where $\mathrm{CBSF}(X, Y)$ is the collimator backscatter factor for jaw setting $X \times Y$, $(\mathrm{MU/Gy})_{\mathrm{calib}}$ the number of MUs per Gy at the treatment unit calibration geometry, D_{calib} the calculated dose in calibration geometry, D_{pre} the calculated dose at the prescription point of the field, and $\mathrm{Gy}_{\mathrm{pre}}$ the prescribed number of Gys at the prescription point. The backscatter to the monitor chamber is assumed to be dependent only on the size of the collimator opening, but not on the position of the opening within the beam. For the treatment units where the MLC is closer to the source than the moving jaws (e.g. Elekta), the backscatter is computed based on the effective size of the MLC opening. The backscatter effect was estimated from the measured output factors for symmetric rectangular fields of size $X \times Y$ as:

$$\mathrm{CBSF}(X, Y) = \frac{D(X, Y)/S_{c,p}(X, Y)}{D(A_{\mathrm{ref}})/S_{c,p}(A_{\mathrm{ref}})}, \tag{4.19}$$

where $D(X, Y)$ is the calculated dose, $S_{c,p}(X, Y)$ the measured output factor, and A_{ref} the reference field size (10×10 cm^2). It is assumed in Eq. (4.19) that the phantom and head scatter effects can be calculated accurately by the developed dose calculation method using an input from the beam model, and that the remaining effects are due to backscatter. Another choice for backscatter modeling is an analytical model, where the amount of backscatter is assumed to be linearly dependent

70

on the irradiated area of the jaw's upper surface [40] or to have a polynomial dependence on the jaw positions [71]. Determination of the parameters would require either in-air collimator scatter factor measurements S_c [40] or intensive MC simulations [71], whereas the method proposed requires only output factors $S_{c,p}$ in water, which have typically already been acquired for the commissioning purposes of PBC.

4.3   Incorporating the beam model with a Monte Carlo based dose calculation method

MC based dose calculation methods are widely recognized to be the most accurate methods currently available, and due to continuous advances in computer technology and algorithms, they are starting to be fast enough for clinical use. However, modeling of the radiation output of the linac is a major challenge. Full simulation through the treatment head of the linac is one option, but it requires a time-consuming manual tuning of e.g. the electron beam parameters to match measured beam properties and a detailed knowledge of the treatment head composition. Hence, the MSM together with its automatic adaptation procedure described in sections 4.1 and 4.2 is more practical alternative. This approach makes it also possible to use the MC based method as a reference for the developed kernel-based method, and therefore to study its limitations in tissue heterogeneities using realistic beams. Since the MC based methods simulate individual particle interactions, a procedure to sample the individual particles from the MSM is needed. Although virtual source models have been widely used for the MC transport algorithms [40, 42], the author of this thesis is not aware that the same source model would have been previously used for both a convolution/superposition and a MC method.

The developed calculation process utilizing the Voxel Monte Carlo (VMC++) transport code [72] consists of three phases (see Fig. 18(a)): (1) sampling of the particles from the MSM, (2) transport of the particles through the static accessory modules, and (3) transport of the particles through the patient volume defined by a CT image. Between the phases (1) and (2), the sampled particles are projected to the starting plane of the topmost accessory, and after exiting the last accessory module, they are projected to the patient surface. Hence, only the open beam part of the MSM is used, whereas hard wedges, compensators, blocks and MLC are modeled by performing a direct particle transport. Each accessory module specifies the shape and material composition of the corresponding accessory. Using the proposed approach, a good agreement to the measurements was obtained without further modifications to the model. Direct transport through the accessories was chosen, since then the complex effects, such as the TG design of the MLC and the scatter from the wedge, can be modeled accurately in a simple way. Dynamic accessories, such as the EDW, are modeled by sampling randomly the instances of a dynamic
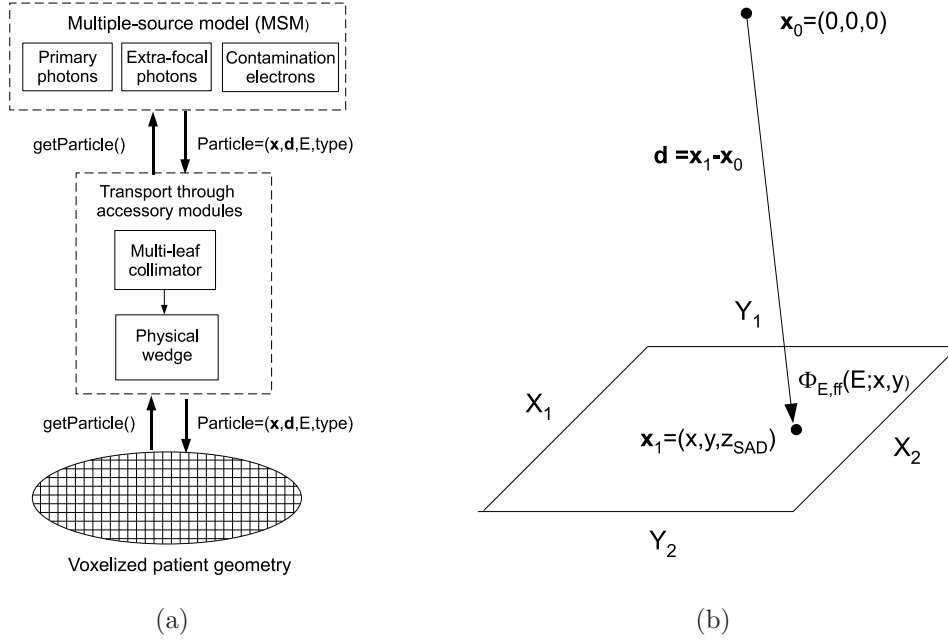
Fig. 18: (a) A block diagram of the developed calculation process. (b) Sampling of the particles from the primary photon source.

geometry based on the device trajectory as a function of MUs, and by performing a transport with a small number of particles for each instance.

Since the sub-source weights of the original MSM are defined as fractions of emitted energy, it is necessary to convert them to fractions of emitted particles for MC based calculation. The energy weight $w_{i,\mathrm{e}}$ for sub-source i $(i = 1, \ldots, 3)$ can be computed from the source model information as:

$$w_{i,\mathrm{e}} = \frac{E_i}{\sum_j E_j} = \frac{\int_S \Psi_i(\mathbf{x})\mathrm{d}\mathbf{x}}{\sum_j \int_S \Psi_j(\mathbf{x})\mathrm{d}\mathbf{x}}, \tag{4.20}$$

where E_i is the energy emitted by the ith sub-source, and $\mathbf{x}$ is a 2D vector on the plane S from which the particles are sampled in the MC method. For the primary photon source, S equals the jaw opening, and for the extra-focal photon source, S is a spherical surface slightly larger than the jaw opening. However, Eq. (4.20) cannot be used for the electron contamination source, since it is not possible to obtain an energy fluence in units comparable to the other two sub-sources from the MSM, as the source strength is implicitly included in the curve $c_\mathrm{e}(z)$. Analogously, the particle weight $w_{i,\mathrm{p}}$ for sub-source i $(i = 1, \ldots, 3)$ is defined as:

$$w_{i,\mathrm{p}} = \frac{N_i}{\sum_j N_j}, \tag{4.21}$$

where N_i is the number of particles emitted from ith sub-source. Thus, the particle

and energy weights are related as:

$$w_{i,\text{p}} \propto N_i = \frac{E_i}{\bar{E}_i} = \frac{w_{i,\text{e}} \sum_j E_j}{\bar{E}_i} \tag{4.22}$$

where $\bar{E}_i$ is the mean energy of the particles emitted from ith sub-source.

For each particle used as an input in the MC transport code, the initial position ($\mathbf{x}$), direction ($\mathbf{d}$), energy (E) and particle type (photon or electron) need to be determined. The sub-source i is sampled based on the relative weights $w_{i,\text{p}}$: sub-source i is selected if $P_{i-1} \leq r < P_i$, where $r \sim U(0,1)$, $P_i = \sum_{j=1}^{i} w_{j,\text{p}}$ and $P_0 = 0$. First, in a case of the primary photon source, the particle sampling proceeds in a following way (see Fig. 18(b)):

1. Sample a position (x, y) at the isocenter plane uniformly from a rectangle defined by current jthe aw settings (X_1, X_2, Y_1, Y_2) i.e. $x = X_1 + r(X_2 - X_1)$ and $y = Y_1 + s(Y_2 - Y_1)$, where $r, s \sim U(0,1)$.
2. Account for a non-uniform particle fluence distribution $\Phi_{\text{prim}}(x, y)$ using the rejection sampling technique [73]: Sample a random number $r \sim U(0,1)$. If $r < \Phi_{\text{prim}}(x, y) / \max_{x,y}\{\Phi_{\text{prim}}(x, y)\}$, accept the particle and proceed to the step (3), otherwise return to the step (1).
3. Since the coordinates of the target are $\mathbf{x}_0 = (0, 0, 0)$, the direction for the particle is obtained as $\mathbf{d} = (x, y, z_{\text{SAD}})$, where z_{SAD} is the source-to-axis distance. The position $\mathbf{x}$ at the surface of the topmost accessory is obtained via projection from $\mathbf{x}_0$ along the direction $\mathbf{d}$.
4. Calculate the radial distance from beam CAX as $R = \sqrt{x^2 + y^2}$, and determine the corresponding particle fluence spectrum $\Phi_{E,\text{ff}}(E; R)$. Then, sample the energy E using the inverse transform sampling [73] for a piece-wise linear spectrum function $\Phi_{E,\text{ff}}(E; R)$.

Secondly, in a case of the extra-focal photon source, each point on the finite-sized plane acts as an isotropic source of radiation. To obtain uniform distribution of particles on the surface of a sphere, the azimuthal (θ) direction angle must be sampled from a uniform distribution and the polar angle (ϕ) from a distribution $\phi = \cos^{-1}(2v - 1)$, where v follows the uniform $U(0,1)$ distribution. For a single source point, it therefore holds that $\Phi_{\text{ef}}(\theta, \phi) \propto 1$ as the mean energy is spatially invariant. Hence, no fluence correction is needed for extra-focal photons in the sampling process. In the sampling routine, an initial position (x, y) is sampled from a 2D Gaussian with the standard deviation of σ_{ef}. Then the direction is obtained by sampling the angles ϕ and θ isotropically as was described above. After the particle has been projected to the topmost accessory plane, it is checked if the particle trajectory intersects with the jaws. If so, the sampling process returns to the

sub-source selection phase. Otherwise, the energy E is sampled from the spatially constant spectrum $\Phi_{E,\text{ef}}(E)$ using an inverse transform sampling technique [73].

The MSM described in Sec. 4.1 does not include a spectrum or a weight for the contamination electrons due to the simple energy deposition mechanism in the kernel-based calculation method, but they both can be derived from the curve $c_{\text{e}}(z)$. To derive the spectrum $\Phi_{E,\text{el}}$, the curve $c_{\text{e}}(z)$ is converted into a PDD curve ($\text{PDD}_{\text{e,target}}$) by accounting for the convolution with the two Gaussians. The spectrum of contamination electrons was simulated for three nominal energies (6, 10 and 15 MV) using BEAMnrc. These spectra are then used as templates, from which the one having nominal energy closest to the current beam is selected. The energy axis of the template spectrum is scaled by a factor, which minimizes the squared error between $\text{PDD}_{\text{e,target}}$ and $\text{PDD}_{\text{e,curr}}$, which is computed as a weighted sum of pre-calculated monoenergetic electron PDDs that were simulated with the VMC++. The energy weight can then be computed as $w_{\text{el,e}} = \int_{z=0}^{\infty} c_{\text{e}}(z)\mathrm{d}z / E_{\text{pb}}$, where E_{pb} is the total energy of a pencil beam in the kernel-based method. In the particle sampling process, first a position (x, y) is sampled from the dual Gaussian distribution: if $r < c_1$, the first Gaussian is used, and otherwise the second Gaussian is selected; $r \sim U(0, 1)$. A non-uniform particle fluence is accounted for by applying the rejection sampling technique, which is similar to the process for the primary photon source. Then the direction $\mathbf{d}$ is determined by sampling a position from a jaw opening visible from the sampled source position (x, y). Finally, the electron energy is sampled similarly to the other sub-sources.

5 Verifying the accuracy of the developed methods

The methods developed in this thesis have been verified by extensive comparisons against dosimetric measurements and MC simulations. In this chapter, a summary of the major results is given. More detailed results can be found from **II**, **III**, **IV**, **V** (mainly utilizing ionization chamber measurements) and from **I** (using MC simulations as a reference).

5.1 Comparisons against measurements

The first requirement for a dose calculation system is to obtain a good agreement with the basic measurement data that have been used for deriving the beam model parameters. For open fields the agreement between the ionization chamber measurements (PDDs and profiles) and the AAA dose calculations was found to be generally better than 2%/2 mm [**II**]. However, slightly larger deviations were observed for a few points close to the field edge. Similar results were obtained for Varian, Elekta and Siemens treatment units, for all studied nominal energies $(6, \ldots, 23 \text{ MV})$, and for FFF beams. See Fig. 19 for a typical comparison using the basic beam data. For hard wedges, the agreement was found to be similar to open fields [**III**], although the errors in the build-up region were slightly larger. Hence, the results for open and wedged fields fulfill the acceptability criteria (2%/2 mm for open fields, 3%/3 mm for wedged fields) in simple geometries proposed by Venselaar et al. [74]. Compared to PBC, the results in the region around the field penumbra, where there is a significant contribution from the extra-focal photons, are notably better with AAA. When the beam model was incorporated with the VMC++ algorithm in **IV**, an agreement of 2%/2 mm was achieved for open fields and 3%/3 mm for wedged fields, giving an increased evidence that the beam model provides a realistic description of the treatment beam.

In addition to reproducing the basic beam data, also the generalized beam setups (various SSDs, irregular beam shapes) must be accurately modeled. For open fields with the SSDs in the range of $80, \ldots, 120$ cm, the observed deviations have been generally within 2%/2 mm, except for a high nominal energy and a short SSD, where deviations in the build-up region increase to about 3%/3 mm [**II**, **III**]. For hard wedges, there were substantial differences in the build-up region for short SSDs particularly for the high beam energy (18 MV) when the AAA version of 7.5.14.3 was used in **III**. However, this problem has been addressed in more recent AAA versions (8.8 and later) by improving the beam model and the process for deriving the beam model parameters for wedges. The wedge PDDs calculated with the AAA version 8.8.17 are illustrated in Fig. 20, which shows clear improvements to the results
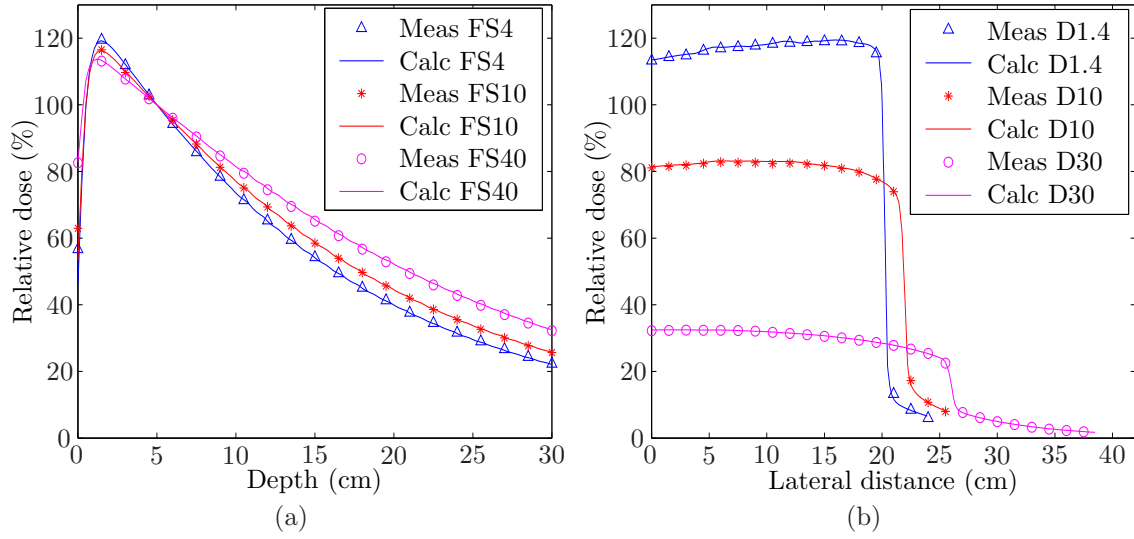
Fig. 19: Comparison between the calculations and the measurements used in the optimization of the beam model parameters for a Varian 6 MV beam. Dose distributions have been normalized to 100% at 5 cm depth on the CAX. (a) PDDs for the field sizes of 4×4, 10×10, and 40×40 cm^2. (b) Profiles for the field size 40×40 cm^2 at the depths of 1.4, 10, and 30 cm.

presented in Fig. 8 in **III**. For the tested irregularly-shaped MLC apertures, the measured and the calculated absolute point doses agreed within 1% in the center of the field [**II**]. Also the depth doses in absolute scale for square-shaped MLC collimated fields agreed within 2%/2 mm [**III**]. These results fulfill well the 3% criterion, which is set for the irregular fields [74]. For the asymmetrically centered fields, the absolute doses at the center of the field were within 3% for open fields, and within 4% for wedged fields [**II**, **III**], fulfilling again the acceptability criteria (3% for open and 4% for wedged asymmetric fields) [74]. The verification tests performed for the MC based calculation system presented in **IV** were more limited, but the absolute dose agreement for the irregular MLC apertures was similar to that of AAA (errors were within 1.5%).

IMRT and EDW fields provide additional test cases for the calculation system, since the calculation of these fields is based on the beam model for the open field. For the IMRT, the dose calculation also involves the computation of an actual fluence from leaf motions, which is performed by a separate module in Eclipse^{TM} TPS. For the EDW, AAA reproduces measurements of symmetric and asymmetric fields of varying sizes generally with 2%/2 mm accuracy [**III**]. The IMRT calculation has been tested by using 1-cm-wide sweeping gaps generating square fluence patterns of sizes from 4×4 to 10×10 cm^2 [**III**]. After d_{max}, the agreement in the depth doses in an absolute scale was within 1%/1 mm for both AAA and PBC. However, AAA was able to reproduce the build-up region better than PBC for the small fluence sizes. In addition, the calculation of a dynamic chair-shaped field [75] and a clinical
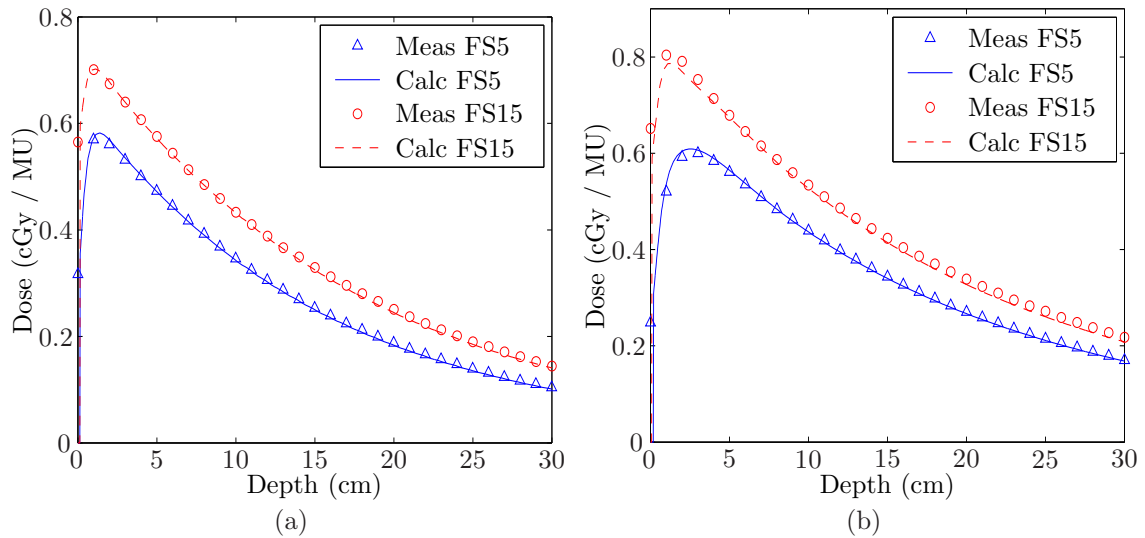
76

Fig. 20: Comparison of the measured and the calculated depth doses (cGy/MU) for a 60 degree wedge at the SSD of 80 cm for a Varian linac. (a) Depth doses for the field sizes of 5×5 and 15×15 cm^2 for a 6 MV beam, (b) the same comparison for an 18 MV beam. The error close to the d_{max} of 15×15 cm^2 field for 18 MV is approximately 2.5%.

head-and-neck field were compared against a 2D ion chamber array measurement [**III**]. For both fields, the errors were within the clinical tolerances (2%/2 mm or 3%/3 mm) inside the modulated area of the field.

The ability of the dose calculation algorithm to model heterogeneous tissues is very important e.g. in lung cancer treatments. In **III**, the measurements were performed in two different phantoms containing a cork insert, which simulates the effect of lung. More clinical situation was tested by using a thorax region of an antropomorphic phantom with embedded ion chambers. Profiles were measured with film and the PDDs with ion chamber in the phantoms with cork inserts. However, care should be taken when interpreting the ionization chamber measurements in cork, since the presence of the chamber may cause perturbations in the order of $6, \ldots, 12\%$ to the absorbed dose [76]. This is due to the severe loss of lateral CPE in the beam CAX, and therefore the cavity theories relating the dose in air to the dose in surrounding medium are not valid. This aspect was not fully realized at the time of writing of **III**, and hence the conclusions about the accuracy in heterogeneities presented therein are inaccurate. Better image of the calculation accuracy in heterogeneous tissues can be obtained from the MC simulations performed in **I**, which will be summarized in Sec. 5.2. However, it can be clearly observed that the cork insert has only a small effect on the PBC calculations utilizing modified Batho correction, while its effect on the AAA calculations is significant especially for small field sizes. From the profile measurements, it can be seen that the lateral water-cork interface is reasonably well modeled with the AAA in general, providing a significant improvement over the PBC, especially in the tail region of profiles in cork.

5.2 Comparisons against Monte Carlo simulations

Due to the dosimetric challenges in the presence of heterogeneities, the accuracy of AAA in low- and high-density heterogeneities was verified using MC simulations in **I**. The phantoms simulating lung were the same as those in **III**, and similar inserts with smaller thicknesses were used to simulate the effect of bone. The deviations between the AAA calculations and the MC simulations were smaller than the 3%/3 mm criterion [74] for all but one test case. For the smallest field of 3×3 cm^2 for the 18 MV beam in a phantom containing a slab-like low-density insert, deviations up to 8% were observed. This is a limitation of the used rectilinear density scaling method, and similar discrepancies have been reported also in the 3D point-spread-kernel based approaches [26]. A comparison of measured and calculated PDDs in a phantom with a low-density insert are shown in Fig. 21. When comparing to the PBC calculations of the same phantom presented in **III**, the AAA calculations agree significantly better with the MC simulations, particularly for the small field sizes with both 6 and 18 MV energy modes.
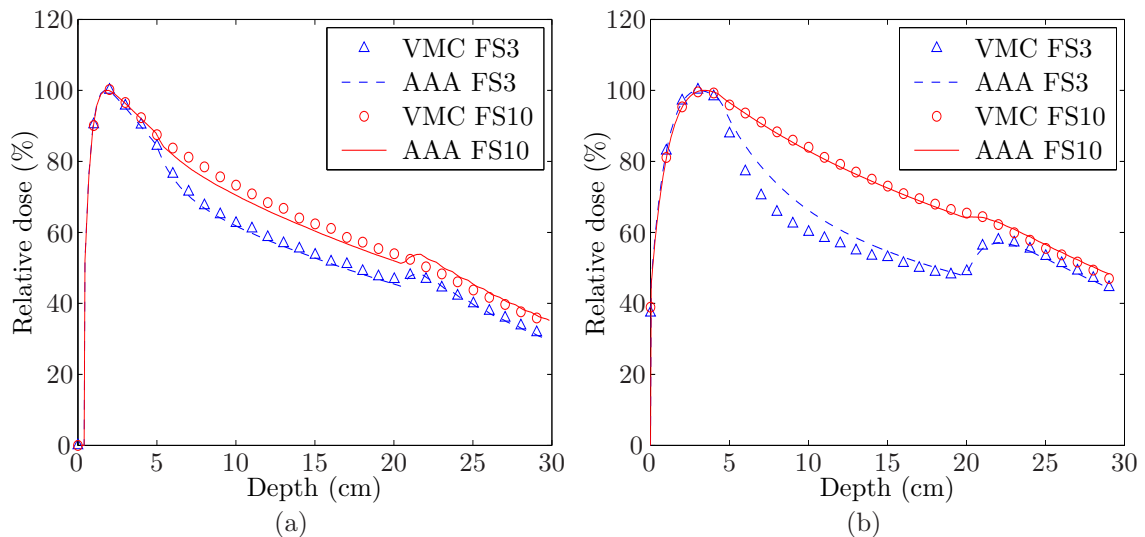

Fig. 21: Comparison of the PDDs calculated with a kernel-based method (AAA) and with a MC method (VMC) for the field sizes of 3×3 and 10×10 cm^2 in a water phantom containing a low-density insert ($\rho_w = 0.3$) in case of (a) 6 MV beam and (b) 18 MV beam.

6 Summary and discussion

As the first aim of the thesis, a dose calculation algorithm based on the superposition of MC simulated pencil-beam kernels was developed [**I**]. In this algorithm, the calculation of absorbed dose in the patient is viewed as a superposition of pencil-beams weighted with the energy fluence distribution of the beam. During the dose calculation process, the pencil-beam is divided into a lateral and a depth-directed component, which are separately scaled according to the radiological path length information computed from the CT-image to account for tissue heterogeneities. The scatter can be efficiently calculated using incremental methods, since the lateral component is modeled as a sum of radial exponential functions. To characterize the radiation output of a linac (the second aim), an MSM and an optimization process for adapting the model to an individual treatment unit were developed [**II**]. The MSM consists of three sub-sources for the open beam (primary photon, extra-focal photon, and electron contamination source), and an extra source to model the scatter originating from the wedge filter. Free parameters of the model are determined by minimizing an objective function, which quantifies the deviation between the dose calculations and the basic measurements consisting of PDDs and profiles for several field sizes. As the fourth aim, the beam model was incorporated with an MC based algorithm [**IV**].

The beam model and the kernel-based dose calculation method were integrated into a commercial Eclipse^{TM} Integrated TPS as an AAA method. The commercial algorithm was verified against a comprehensive set of measurements and MC simulations in **I** and **III** (third aim). The accuracy of the developed dose calculation system fulfills the common clinical acceptability criteria [74] in most of the studied situations. It was also shown that the modeling in the region around the field penumbra and in heterogeneous tissues is significantly better than with that of a widely used PBC method. The calculation time of the developed method is similar or better than that of PBC. However, the deviations in a lung geometry for a small field size (3×3 cm^2) with large nominal energy (18 MV) exceeded the acceptability criterion of 3% [74] as differences up to 8% were detected inside the medium simulating lung. Although similar discrepancies have been reported for the methods that utilize 3D point-spread kernels [26], this discrepancy may limit the clinical use of the method in the planning of lung cancer treatments with high energy beams. To obtain acceptable accuracy also in the cases of severe electron disequilibrium, a method based on the first principles, such as MC or direct solving of the Boltzmann transport equations [31,32], should be applied. However, beam modeling will remain a challenge, and the methods presented in this thesis are viable approaches for this problem.

The modeling of electron contamination is the most empirical part of the MSM. The development of more physics-based model for the electron contamination is expected to result in improvements of calculation accuracy in the build-up region for open and wedged fields, especially in a case of short SSDs. The desired model would describe the influence of the beam limiting devices, as well as the air column for all common situations. However, no parameterized model suitable for kernel-based dose calculations, which would be general enough to handle all common situations (e.g. different SSDs and accessories) has been proposed so far, although advancements have recently been made for MC methods [77] and for PDD calculations [78]. To further improve the accuracy for asymmetric fields, which is already clinically acceptable, an analytical model could be used to characterize backscatter into the monitor chamber [40]. The optimization of the parameters for the backscatter model should then be performed simultaneously to the other parameters. As compensator-based IMRT is gaining popularity at some institutions e.g. due to the finer spatial resolution and more efficient delivery compared to MLC-based IMRT [79], the developed beam model should be enhanced to account for spectrum changes and scatter caused by the physical compensator. The modeling of FFF beams could be also improved by implementing a special extra-focal source, such as a planar annulus source with a constant intensity, as proposed by Yang et al. [41].

If desired, the calculation time of kernel-based method could be further decreased by using a multiple resolution levels in the 2D scatter phase, where the number of levels would be dependent on the range of the exponential component. The fitting of the exponential functions to the MC data, which is currently done for each patient dose calculation, could be performed as a pre-calculation step to obtain an additional speed gain. If the MC based calculation method developed in this thesis would be implemented into a TPS, the geometry modules for different types of MLCs and wedges would need to be reconstructed based on the specifications given by different manufacturers. It might be possible to improve the calculation accuracy of the kernel-based method in heterogeneous phantoms by applying the methodology of Keall and Hoban [62], where the full electron density distribution between the interaction and the deposition sites is taken into account. However, due to the nature of pencil-beam based method, that correction would have to be separately applied for both the depth-directed and the lateral component.

7 Conclusions

In this thesis, it was shown that the proposed dose calculation method, which is based on the superposition of MC simulated pencil-beam kernels, has an accuracy, which makes it applicable for clinical megavoltage photon beam treatment planning in a wide range of conditions. In addition, the calculation times (in the order of 10 s per field) are fast enough to enable multiple re-calculations during the planning phase. The only major limitation of the method is its inaccuracy for a high-energy beam of a small field size in lung tissue. Even so, the method developed here provides significant improvements in the accuracy compared to a currently widely used semi-empirical method, being on the same level as typically slower methods, which are based on the use of 3D point spread kernels. When using a physics-based MSM to characterize the treatment beam, it was shown that it is possible to derive automatically the free parameters of the model from a rather simple set of beam data measurements using optimization methods. This allows an easy adoption of the proposed dose calculation system in the clinics, since no manual tuning of the various parameters of the beam model is required. It was also demonstrated that the developed beam model can be attached to another modern dose calculation algorithm, such as MC, if more accuracy is required for the patient dose calculation part.

The survival rates of many cancers have improved continuously throughout the last thirty years [80], and this development is expected to continue in the future. Although it is difficult to separate the contribution of each factor to the improved treatment outcome, the adoption of more accurate dose prediction methods is surely one important factor in this progress Hence, the research and development of even more accurate methods to predict the delivered dose should be encouraged. Possible future advancements include the adoption of MC or Boltzmann equation solvers for clinical dose calculation, and the development of methods capable of predicting the dose for a moving anatomy. In the latter case, the goal is to accumulate the dose to a reference CT-image from the doses calculated to several CT images, which represent snapshots of the patient anatomy in the presence of organ motion.

References

[1] G. M. Ross. Induction of cell death by radiotherapy. *Endocr. Relat. Cancer*, 6:41–44, 1999.

[2] B. A. Fraass. The development of conformal radiation therapy. *Med. Phys.*, 22:1911–1921, 1995.

[3] W. J. Meredith. 40 years of development in radiotherapy. *Phys. Med. Biol.*, 29:115–120, 1984.

[4] D. I. Thwaites and J. B. Tuohy. Back to the future: the history and development of the clinical linear accelerator. *Phys. Med. Biol.*, 51:R343–R362, 2006.

[5] J. C. Ganz. *Gamma knife surgery*. Springer-Verlag, 1997.

[6] C. J. Karzmark and N. C. Pering. Electron linear accelerators for radiation therapy: history, principles and contemporary developments. *Phys. Med. Biol.*, 18:321–354, 1973.

[7] S. Webb. *The physics of conformal radiotherapy: advances in technology*. Institute of Physics Publishing, 1997.

[8] J. R. Clarkson. A note on depth doses in fields of irregular shape. *Br. J. Radiol.*, 14:265–268, 1941.

[9] W. J. Meredith and G. J. Neary. The production of isodose curves and the calculation of energy absorption from stardard depth dose data. *Br. J. Radiol.*, 17:126–130, 1944.

[10] A. Ahnesjö and M. M. Aspradakis. Dose calculations for external photon beams in radiotherapy. *Phys. Med. Biol.*, 44:R99–R155, 1999.

[11] J. R. Cunningham. Scatter-air ratios. *Phys. Med. Biol.*, 17:42–51, 1972.

[12] P. Storchi and E. Woudstra. Calculation of the absorbed dose distribution due to irregularly shaped photon beams using pencil beam kernels derived from basic beam data. *Phys. Med. Biol.*, 41:637–656, 1996.

[13] P. R. M. Storchi, L. J. van Battum, and E. Woudstra. Calculation of a pencil beam kernel from measured photon beam data. *Phys. Med. Biol.*, 44:2917–2928, 1999.

[14] H. F. Batho. Lung corrections in cobalt 60 beam therapy. *J. Can. Assoc. Radiol.*, 15:79–83, 1964.

[15] M. R. Sontag and J. R. Cunningham. Clinical application of a CT based treatment planning system. *Comput. Tomogr.*, 2:117–130, 1978.

[16] M. R. Sontag and J. R. Cunningham. The equivalent tissue-air ratio method for making absorbed dose calculations in a heterogeneous medium. *Radiology*, 129:787–794, 1978.

[17] R. Mohan, C. Chui, and L. Lidofsky. Differential pencil beam dose computation model for photons. *Med. Phys.*, 13:64–73, 1986.

[18] A. L. Boyer and E. C. Mok. A photon dose distribution model employing convolution calculations. *Med. Phys.*, 12:169–177, 1985.

[19] T. R. Mackie, J. W. Scrimger, and J. J. Battista. A convolution method of calculating dose for 15-MV x rays. *Med. Phys.*, 12:188–196, 1985.

[20] A. Ahnesjö. Collapsed cone convolution of radiant energy for photon dose calculation in heterogeneous media. *Med. Phys.*, 16:577–592, 1989.

[21] A. Ahnesjö, M. Saxner, and A. Trepp. A pencil beam model for photon dose calculation. *Med. Phys.*, 19:263–73, 1992.

[22] J. D. Bourland and E. L. Chaney. A finite-size pencil beam model for photon dose calculations in three dimensions. *Med. Phys.*, 19:1401–1412, 1992.

[23] T. Bortfeld, W. Schlegel, and B. Rhein. Decomposition of pencil beam kernels for fast dose calculations in three dimensional treatment planning. *Med. Phys.*, 20:311–318, 1993.

[24] O. Z. Ostapiak, Y. Zhu, and J. Van Dyk. Refinements of the finite-size pencil beam model of three-dimensional photon dose calculation. *Med. Phys.*, 24:743–750, 1997.

[25] M. Nilsson and T. Knöös. Application of the Fano theorem in inhomogeneous media using a convolution algorithm. *Phys. Med. Biol.*, 37:69–83, 1992.

[26] M. R. Arnfield, C. Hartmann Siantar, J. Siebers, P. Garmon, L. Cox, and R. Mohan. The impact of electron transport on the accuracy of computed dose. *Med. Phys.*, 27:1266–1274, 2000.

[27] I. Kawrakow. Accurate condensed history Monte Carlo simulation of electron transport. I.EGSnrc, the new EGS4 version. *Med. Phys.*, 27:485–98, 2000.

[28] I. Kawrakow and M. Fippel. VMC++, a fast MC algorithm for Radiation Treatment planning. *Proc. 13th Int. Conf. on the Use of Computers in Radiation Therapy (ICCR). Springer.*, 2000.
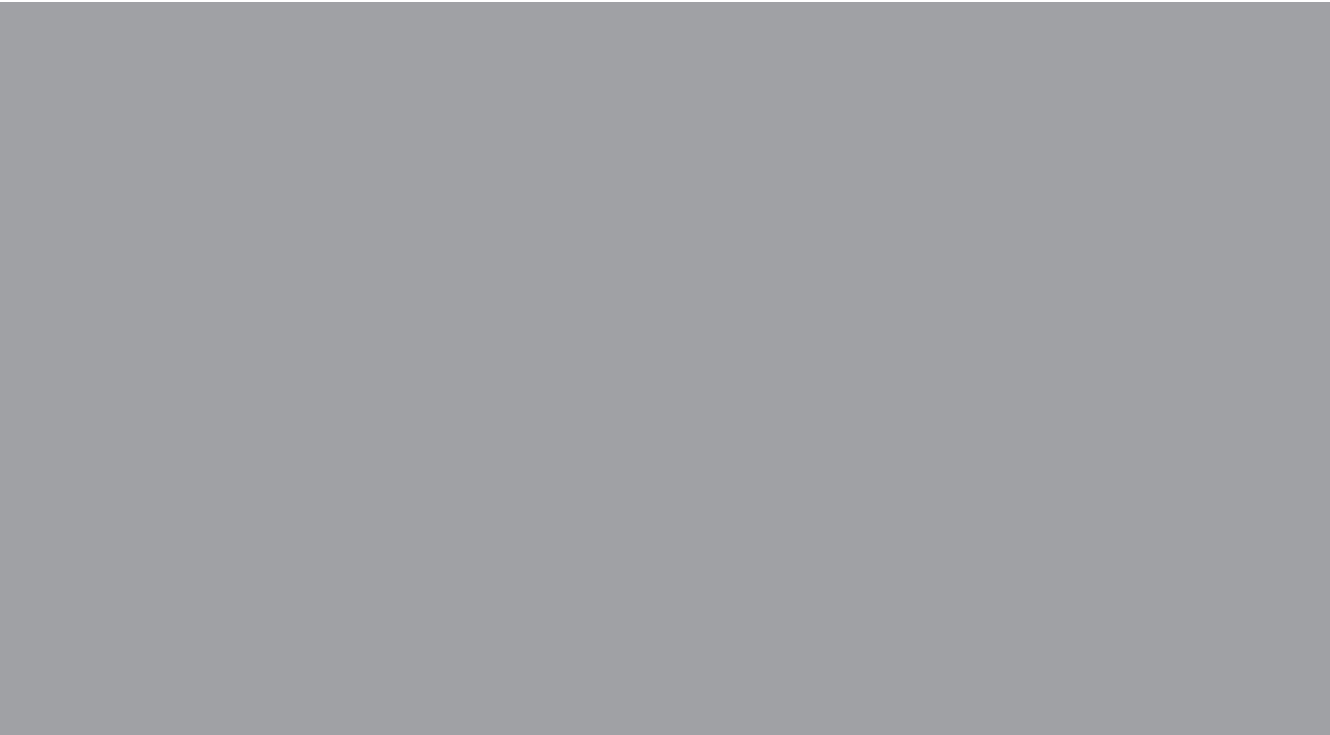
[29] P. Andreo and A. Brahme. Restricted energy loss straggling and multiple scattering of electrons in mixed Monte Carlo procedures. *Radiat. Res.*, 100:16–29, 1984.

[30] A. F. Bielajew and D. W. O. Rogers. PRESTA: The parameter reduced electron-step transport algorithm for electron Monte Carlo transport. *Nucl. Instrum. Methods B*, 18:165–181, 1987.

[31] K. A. Gifford, J. L. Horton, T. A. Wareing, G. Failla, and F. Mourtada. Comparison of a finite-element multigroup discrete-ordinates code with Monte Carlo for radiotherapy calculations. *Phys. Med. Biol.*, 51:2253–2265, 2006.

[32] T. Wareing, O. Vassiliev, G. Failla, I. Davis, J. McGhee, D. Barnett, J. Horton, and F. Mourtada. TU-EE-A1-01: Validation of a prototype deterministic solver for photon beam dose calculations on acquired CT data in the presence of narrow neams and heterogeneities. *Med. Phys.*, 34:2565, 2007.

[33] D. W. Rogers, B. A. Faddegon, G. X. Ding, C. M. Ma, J. We, and T. R. Mackie. BEAM: a Monte Carlo code to simulate radiotherapy treatment units. *Med. Phys.*, 22:503–524, 1995.

[34] S. A. Naqvi, W. D. D'Souza, M. A. Earl, S. J. Ye, R. Shih, and X. A. Li. Using a photon phase-space source for convolution/superposition dose calculations in radiation therapy. *Phys. Med. Biol.*, 50:4111–4124, 2005.

[35] D. Sheikh-Bagheri and D. W. O. Rogers. Sensitivity of megavoltage photon beam Monte Carlo simulations to electron beam and other parameters. *Med. Phys.*, 29:379–390, 2002.

[36] A. E. Schach von Wittenau, L. J. Cox, P. M. Jr. Bergstrom, W. P. Chandler, C. L. Hartmann Siantar, and R. Mohan. Correlated histogram representation of Monte Carlo derived medical accelerator photon-output phase space. *Med. Phys.*, 26:1196–1211, 1999.

[37] I. Chetty, J. J. DeMarco, and T. D. Solberg. A virtual source model for Monte Carlo modeling of arbitrary intensity distributions. *Med. Phys.*, 27:166–172, 2000.

[38] M. K. Fix, P. J. Keall, K. Dawson, and J. V. Siebers. Monte Carlo source model for photon beam radiotherapy: photon source characteristics. *Med. Phys.*, 31:3106–3121, 2004.

[39] H. H. Liu, T. R. Mackie, and E. C. McCullough. A dual source photon beam model used in convolution/superposition dose calculations for clinical megavoltage x-ray beams. *Med. Phys.*, 24:1960–1974, 1997.

[40] S. B. Jiang, A. L. Boyer, and C. M. Ma. Modeling the extrafocal radiation and monitor chamber backscatter for photon beam dose calculation. *Med. Phys.*, 28:55–66, 2001.

[41] Y. Yang, L. Xing, A. L. Boyer, Y. Song, and Y. Hu. A three-source model for the calculation of head scatter factors. *Med. Phys.*, 29:2024–2033, 2002.

[42] M. Fippel, F. Haryanto, O. Dohm, F. Nusslin, and S. Kriesen. A virtual photon energy fluence model for Monte Carlo dose calculation. *Med. Phys.*, 30:301–311, 2003.

[43] A. Ahnesjö, L. Weber, A. Murman, M. Saxner, I. Thorslund, and E. Traneus. Beam modeling and verification of a photon beam multisource model. *Med. Phys.*, 32:1722–1737, 2005.

[44] F. M. Khan. *The physics of radiation therapy.* Williams & Wilkins Baltimore, 1994.

[45] E. B. Podgorsak, editor. *Radiation oncology physics: a handbook for teachers and students.* International Atomic Energy Agency, Vienna, 2005.

[46] M. J. Berger, J. H. Hubbell, S. M. Seltzer, J. Chang, J. S. Coursey, R. Sukumar, and D. S. Zucker. XCOM: Photon Cross Sections Database, NIST Standard Reference Database 8 (XGAM). Available from: URL: http://physics.nist.gov/PhysRefData/Xcom/Text/XCOM.html.

[47] F. H. Attix. Energy-absorption coefficients for γ-rays in compounds or mixtures. *Phys. Med. Biol*, 29:869–871, 1984.

[48] F. H. Attix. Energy imparted, energy transferred and net energy transferred. *Phys. Med. Biol.*, 28:1385–1390, 1983.

[49] J. Dutreix, A. Dutreix, and M. Tubiana. Electronic equilibrium and transition stages. *Phys. Med. Biol.*, 10:177–190, 1964.

[50] J. E. O'Connor. The variation of scattered x-rays with density in an irradiated body. *Phys. Med. Biol.*, 1:352–369, 1957.

[51] U. Fano. Note on the Bragg-Gray cavity principle for measuring energy dissipation. *Radiat. Res.*, 1:237–240, 1964.

[52] M. R. Sontag and J. R. Cunningham. Corrections to absorbed dose calculations for tissue inhomogeneities. *Med. Phys.*, 4:431–436, 1977.

[53] Varian Medical Systems, Inc., 3100 Hansen Way, Palo Alto, CA 94304-1030, USA. *Eclipse Algorithms Reference Guide (P/N B501813R01A)*, 2008.

[54] J. J. van Gasteren, S. Heukelom, H. J. van Kleffens, R. van der Laarse, J. L. Venselaar, and C. F. Westermann. The determination of phantom and collimator scatter components of the output of megavoltage photon beams: measurement of the collimator scatter part with a beam-coaxial narrow cylindrical phantom. *Radiother. Oncol.*, 20:250–257, 1991.

[55] J. L. M. Venselaar, J. J. M. van Gasteren, S. Heukelom, H. N. Jager, B. J. Mijnheer, R. van der Laarse, H. J. van Kleffens, and C. F. Westermann. A consistent formalism for the application of phantom and collimator scatter factors. *Phys. Med. Biol.*, 44:365–381, 1999.

[56] P. Storchi and E. Woudstra. Calculation models for determining the absorbed dose in water phantoms in off-axis planes of rectangular fields of open and wedged photon beams. *Phys. Med. Biol.*, 40:511–527, 1995.

[57] P. Storchi and J. J. M. van Gasteren. A table of phantom scatter factors of photon beams as a function of the quality index and field size. *Phys. Med. Biol.*, 41:563–571, 1996.

[58] E. El-Khatib and J. J. Battista. Improved lung dose calculation using tissue-maximum ratios in the batho correction. *Med. Phys.*, 11:279–286, 1984.

[59] S. J. Thomas. A modified power-law formula for inhomogeneity corrections in beams of high-energy x-rays. *Med. Phys.*, 18:719–723, 1991.

[60] W Ulmer, J Pyyry, and W Kaissl. A 3D photon superposition/convolution algorithm and its foundation on results of Monte Carlo calculations. *Phys. Med. Biol.*, 50:1767–90, 2005.

[61] W. H. Press, S. A. Teukolsky, W. T. Vetterling, and B. P. Flannery. *Numerical recipes in C: the art of scientific computing.* Cambridge University Press, third edition, 2007.

[62] P. Keall and P. Hoban. Accounting for primary electron scatter in x-ray beam convolution calculations. *Med. Phys.*, 22:1413–1418, 1995.

[63] A. N. Tikhonov, A. Goncharsky, V. V. Stepanov, and A. G. Yagola. *Numerical methods for the solution of ill-posed problems.* Springer, 1995.

[64] D. A. Jaffray, J. J. Battista A. Fenster, and P. Munro. X-ray sources of medical linear accelerators: focal and extra-focal radiation. *Med. Phys.*, 20:1417–1427, 1993.

[65] A. Ahnesjö, T. Knöös, and A. Montelius. Application of the convolution method for calculation of output factors for therapy photon beams. *Med. Phys.*, 19:295–301, 1992.

[66] D. Sheikh-Bagheri and D. W. O. Rogers. Monte Carlo calculation of nine megavoltage photon beam spectra using the BEAM code. *Med. Phys.*, 29:391–402, 2002.

[67] G. Starkschall, R. E. Steadham, R. A. Popple, S. Ahmad, and I. I. Rosen. Beam-commissioning methodology for a three-dimensional convolution/superposition photon dose algorithm. *J. Appl. Clin. Med. Phys.*, 1:8–27, 2000.

[68] D. A. Low, W. B. Harms, S. Mutic, and J. A. Purdy. A technique for the quantitative evaluation of dose distribution. *Med. Phys.*, 25:656–661, 1998.

[69] M. J. D. Powell. An efficient method for finding the minimum of a function of several variables without calculating derivatives. *Computer J.*, 7:155–162, 1964.

[70] J. A. Nelder and R. Mead. A simplex method for function minimization. *Computer J.*, 7:308–313, 1965.

[71] H. H. Liu, T. R. Mackie, and E. C. McCullough. Modeling photon output caused by backscattered radiation into the monitor chamber from collimator jaws using a Monte Carlo technique. *Med. Phys.*, 27:737–744, 2000.

[72] I. Kawrakow and M. Fippel. VMC++, a fast MC algorithm for radiation treatment planning. In *The Use of Computers in Radiotherapy, XIIIth International Conference, Heidelberg*, pages 126–128, 2000.

[73] C. P. Robert and G. Casella. *Monte Carlo statistical methods*. Springer-Verlag, New York, 2004.

[74] J. Venselaar, H. Welleweerd, and B. Mijnheer. Tolerances for the accuracy of photon beam dose calculations of treatment planning systems. *Radiother. Oncol.*, 60:191–201, 2001.

[75] A. Van Esch, J. Bohsung, P. Sorvari, M. Tenhunen, M. Paiusco, M. Iori, P. Engström, H. Nyströ, and D. P. Huyskens. Acceptance tests and quality control (QC) procedures for the clinical implementation of intensity modulated radiotherapy (IMRT) using inverse planning and the sliding window technique: experience from five radiotherapy departments. *Radiother. Oncol.*, 65:53–70, 2002.

[76] G. X. Ding, D. M. Duggan, and C. W. Coffey. Comment on "Testing of the analytical anisotropic algorithm for photon dose calculation" [Med. Phys. 33, 4130-4148 (2006)]. *Med. Phys.*, 34:3414, 2007.

[77] J. Yang, J. S. Li, L. Qin, W. Xiong, and C. M. Ma. Modelling of electron contamination in clinical photon beams for Monte Carlo dose calculation. *Phys. Med. Biol.*, 49:2657–2673, 2004.

[78] A. Lopez Medina, A. Teijeiro, J. Garcia, and J. Esperon. Characterization of electron contamination in megavoltage photon beams. *Med. Phys*, 32:1281–1292, 2005.

[79] S. X. Chang, T. J. Cullip, K. M. Deschesne, E. P. Miller, and J. G. Rosenman. Compensators: An alternative IMRT delivery technique. *J. Appl. Clin. Med. Phys.*, 5:15–36, 2004.

[80] M. J. Horner, L. A. G. Ries, M. Krapcho, N. Neyman, R. Aminou, N. Howlader, S. F. Altekruse, E. J. Feuer, L. Huang, A. Mariotto, B. A. Miller, D. R. Lewis, M. P. Eisner, D. G. Stinchcomb, and B. K. Edwards (eds). SEER Cancer Statistics Review, 1975-2006. *National Cancer Institute. Bethesda, MD, based on November 2008 SEER data submission, posted to the SEER web site*, 2009.